CALIFORNIA ENERGY COMMISSION

CALIFORNIA NATURAL RESOURCES AGENCY

ENERGY RESEARCH AND DEVELOPMENT DIVISION

FINAL PROJECT REPORT

Gas Storage Safety Monitoring with Advanced Reflectometry Technologies (NGS-SMART)

June 2024| CEC-500-2024-077

PREPARED BY:
Yuxin Wu
Linqing Luo
Jiannan Wang
Lawrence Berkeley National Laboratory
Kenichi Soga
Tianchen Xu
Chien-Chih Wang
University of California, Berkeley
Primary Authors

Jeffrey Sunquist
Project Manager
California Energy Commission

Agreement Number: PIR-19-002

Reynaldo Gonzalez
Branch Manager
ENERGY SYSTEMS & TRANSPORTATION BRANCH

Jonah Steinbuck, Ph.D.
Director
ENERGY RESEARCH AND DEVELOPMENT DIVISION

Drew Bohan
Executive Director

ACKNOWLEDGEMENTS

We would like to express our appreciation to the Pacific Gas & Electric Company for their support of the field logistics, experimentation, and the engineered tests conducted at C-FER Technologies in Edmonton, Canada. We also thank C-FER Technologies for conducting the simulated well tests and Schlumberger for their assistance in field sensor installation. We thank the members of our Technical Advisory Committee for providing insightful comments that help guide the research effort. We also appreciate the help from the UC Pacific Earthquake Engineering Research Center and the Center for Smart Infrastructure for assistance with laboratory experiments. We are grateful for the funding support from the California Energy Commission and the guidance of the Commission Agreement Managers for the duration of this project.

PREFACE

The California Energy Commission's (CEC) Energy Research and Development Division manages the Gas Research and Development Program, which supports energy-related research, development, and demonstration not adequately provided by competitive and regulated markets. These natural gas research investments spur innovation in energy efficiency, renewable energy and advanced clean generation, energy-related environmental protection, energy transmission and distribution and transportation.

The Energy Research and Development Division conducts this public interest natural gas-related energy research by partnering with RD&D entities, including individuals, businesses, utilities and public and private research institutions. This program promotes greater gas reliability, lower costs and increases safety for Californians and is focused in these areas:

- Buildings End-Use Energy Efficiency
- Industrial, Agriculture and Water Efficiency
- Renewable Energy and Advanced Generation
- Natural Gas Infrastructure Safety and Integrity
- Energy-Related Environmental Research
- Natural Gas-Related Transportation

Gas Storage Safety Monitoring with Advanced Reflectometry Technologies (NGS-SMART) is the final report for Contract Number PIR-19-002, conducted by Lawrence Berkeley National Laboratory. The information from this project contributes to the Energy Research and Development Division's Gas Research and Development Program.

For more information about the Energy Research and Development Division, please visit the CEC's research website (www.energy.ca.gov/research/) or contact the Energy Research and Development Division at ERDD@energy.ca.gov.

ABSTRACT

In alignment with California's clean energy and climate goals, this project contributes to enhancing the safety of underground gas storage wells by developing and validating real-time, non-invasive monitoring technologies; particularly, distributed fiber optic sensing and electromagnetic time domain reflectometry. Laboratory tests demonstrated distributed fiber optic sensing's high sensitivity in detecting structural deformations and potential leakages, while electromagnetic time domain reflectometry effectively located damages in well casing material, though further evaluation of its sensitivity to minor changes is needed. Larger scale tests at C-FER Technologies validated the accuracy of distributed fiber optic sensing in locating abnormal thermal signatures and its sensitivity to strain signals during pressure cycling, while electromagnetic time domain reflectometry identified complex casing damage features with some limitations in detecting smaller, distant anomalies. By correlating data with previous well logs for non-intrusive diagnostics, field results at the Pacific Gas and Electric Company site further affirmed the capability of distributed fiber optic sensing for continuous well integrity monitoring, and the potential in operational settings of electromagnetic time domain reflectometry. The project also focused on knowledge transfer through industry collaborations, technical advisory committee, discussions with stakeholders, and preparations for scientific publications. Future recommendations include: further development and demonstration of these technologies at pilot scales, integration into existing underground gas storage infrastructure, ongoing adaptation to diverse conditions, and potential expansion to other aspects of the gas supply chain. This project represents a significant step forward in underground gas storage well monitoring, aligning with California’s sustainable and safe energy infrastructure objectives and offering a model for global application in similar contexts.

Keywords: UGS, underground gas storage, DFOS, distributed fiber optic sensing, EM-TDR, electromagnetic time domain reflectometry, gas well integrity

Please use the following citation for this report:

Wu, Yuxin, Linqing Luo, Jiannan Wang, Tianchen Xu, Chien-Chih Wang, and Kenichi Soga. 2023. “Gas Storage Safety Monitoring with Advanced Reflectometry Technologies (NGS-SMART).” California Energy Commission. Publication Number: CEC-500-2024-077

TABLE OF CONTENTS

LIST OF FIGURES

LIST OF TABLES

Executive Summary

Background

California's energy landscape heavily relies on gas and gas infrastructure, a key component of which, is the storage and management of this resource in underground gas storage facilities. Underground gas storage uses geological formations—accessed from the surface through well casing and tubing placed inside drilled wellbores—to store large volumes of gas ensuring a stable supply for various endpoints including residential properties, industrial factories, commercial offices, and power plants. Underground gas storage acts as a pivotal mechanism that allows for the alignment of supply with oscillations in demand. If not properly maintained, these facilities, while essential, pose risks such as environmental damage and public safety hazards. This project directly addresses these concerns by introducing innovative technologies for monitoring the integrity of underground gas storage wells, thus supporting California's commitment to a safe, sustainable, and efficient energy future.

Project Purpose and Approach

The primary objective of this project was to develop and validate cutting-edge technologies for real-time, non-invasive monitoring of underground gas storage wells. Recognizing the critical nature of well integrity for environmental safety and operational efficiency, the project focused on demonstrating technologies capable of early detection of potential well issues, such as tubing/casing deformation, loss metal, corrosion, and leakage. Results can be used to inform stakeholders in the energy sector, policy makers, and technology adopters. Success was measured by the technologies' precision, reliability, and adaptability to real-world conditions. The approach was a multifaceted one, combining laboratory experiments and field demonstrations to rigorously test and validate two monitoring technologies under various conditions. The first, distributed fiber optic sensing (DFOS) uses fiber optic sensing technology to provide continuous measurements of various conditions such as distributed temperature and strain within the underground gas storage well. The second, electromagnetic time domain reflectometry (EM-TDR) is a technology that uses electromagnetic waves to identify the defects on the casing and tubing directly. While DFOS is a commercially available technology, the project explored new applications of the methods to apply it to borehole monitoring, and also investigated installation techniques, data processing, data storage and management, and data interpretation. EM-TDR is a novel technology being developed at Lawrence Berkeley National Laboratory.

Key Results

The project yielded several significant outcomes, underscoring the potential of these technologies to revolutionize underground gas storage well monitoring:

1. **Local Laboratory Tests:** Laboratory tests were conducted to evaluate the sensitivity of the technologies to structural and mechanical degradations of the wellbore

materials, including the steel casing and tubing placed inside the well, before larger-scale tests were conducted. The summary of the results:

- **DFOS:** Demonstrated high sensitivity and spatial accuracy in detecting structural deformations and potential leakages in wellbores. The technology showed real-time monitoring capabilities, essential for early detection of well issues.
- **EM-TDR:** Proved effective in locating simple damages within the well casing material, critical for preventing leaks and blowouts. EM-TDR's sensitivity to minor changes and anomalies is less clear and needs further evaluation.

2. **C-FER Technologies Test Results:** Larger scale, controlled laboratory tests were conducted at a third-party engineering test laboratory, C-FER Technologies, in Canada. The results are summarized below:
    - **DFOS:** DFOS temperature sensing was able to locate, with high accuracy, abnormal thermal signatures simulating potential thermal signals during leakage events. Additionally, DFOS strain sensing showed high sensitivity to strain signals during pressure cycling simulating normal operation procures. Small local strain anomalies were identified demonstrating its capability to detect local early anomalies that could lead to performance degradation of the system.
    - **EM-TDR:** Under the complex damage patterns during the blind tests, EM-TDR was successful in identifying a fraction of the casing damage features including simulated metal loss, pinholes, pitting, and grooving. The technology was unable to identify some features, particularly those that are small and far away from the signal sources.
3. **Field Results at a Pacific Gas and Electric Company Site:**
    - **DFOS:** In the field, DFOS was effectively implemented, providing continuous monitoring of well integrity. It was able to detect changes in strain and temperature, crucial for monitoring well conditions and operations, and in the long-term, potential failures due to degradation.
    - **EM-TDR:** While less commercially ready, EM-TDR demonstrated its capability in an operational setting, correlating EM-TDR data with previous well logging information to assess well integrity. The technology was able to identify potential well condition issues without direct access to the wellbore, showcasing its utility in nonintrusive diagnostics.

The implications of these results are far-reaching. They suggest that such technologies can be replicated and applied in similar environments, offering significant benefits to ratepayers and the public by enhancing the safety and environmental integrity of underground gas storage facilities.

Knowledge Transfer and Next Steps

A key component of this project was the dissemination of findings and the facilitation of technology adoption. This was achieved through various means:

- **Collaborations and Partnerships:** The project engaged with industry stakeholders, creating a bridge between research and practical application. This included efforts through the technical advisory committee as well as discussion with other stakeholders, such as the California Geologic Energy Management Division.
- **Publications:** Findings from the project are being prepared for publication in scientific journals, reaching a broad spectrum of the academic and professional community.

Based on this research, there are several recommendations:

- Further development and demonstration of the DFOS and EM-TDR technologies via additional tests at pilot scales and through additional funding support from the stakeholders and public agencies.
- Integration of DFOS and EM-TDR technologies into the existing infrastructure of underground gas storage facilities for enhanced operational safety and efficiency.
- Ongoing research and adaptation of these technologies to suit diverse environmental conditions and operational challenges.

There is critical scope for further research. Potential directions include:

- Conducting longer-term field demonstrations, such as continuous monitoring over at least periods of 5 to 10 years, and ideally throughout the lifetime of the boreholes, is essential to evaluate the performance of technologies used for underground gas storage monitoring. This is because new gas storage boreholes or tubing are unlikely to exhibit issues within the first few years after installation. Long-term monitoring projects can validate the capability of these technologies to address potential issues that accumulate over time, such as fatigue, fault movement, or chemical corrosion.
- Expanding the application of these monitoring technologies to other aspects of the gas supply chain, such as pipelines.
- Continual refinement of the technologies to enhance their sensitivity, reliability, and user-friendliness.

In conclusion, this project represents a significant advancement in the field of underground gas storage monitoring. It aligns seamlessly with California's objectives of fostering a sustainable and safe energy infrastructure. The technologies developed have the potential not only to mitigate the risks associated with gas storage but also to serve as a model for similar applications globally, marking a step forward in the journey towards a more secure and environmentally responsible energy future.

CHAPTER 1: Introduction

Underground gas storage (UGS) represents a crucial component of the gas supply chain, acting as a buffer to accommodate the fluctuating needs of end users. This sophisticated technology involves the storage of gas in subterranean geological formations to ensure smooth and reliable delivery of the energy source to various destinations including residential properties, industrial factories, commercial offices, and power plants. This is typically accomplished via an extensive network of interconnected pipelines. UGS acts as a pivotal mechanism that allows for the alignment of supply with the oscillations in demand. During periods of low demand, gas is injected and stored within subsurface geological formations, a process achieved using wellbores. Conversely, when demand surges, the stored gas is withdrawn from the storage formation. This cycle involves a series of steps, including compression, injection, storage, withdrawal, and decompression. It is regulated through adjustments to the pressure within the well (Cornot-Gandolphe, 2013; U.S. DOE, 2016).

However, the storage and handling of gas is not without challenges and hazards (Miyazaki, 2009). The storage well is subjected to repetitive cycles of injection and withdrawal, causing stress on the well structure. This can escalate to severe consequences, including well deformation and fracturing (Rouhbakhsh Arfaee and Sedaee Sola, 2014), and in worst-case scenarios, the risk of well failure. Such failures could lead to disastrous events like gas leakages and large-scale surface blowouts, causing environmental damage and safety hazards. A pertinent example of such a catastrophic event is the incident at California's Aliso Canyon UGS facility in October 2015, which resulted in the release of 90,000 tons of gas (Conley et al., 2016; Freifeld et al., 2016; Zhang et al., 2022).

The well integrity issues are not exclusive to UGS but are also prevalent in conventional oil and gas reservoirs. For instance, over 300 wells in California's Wilmington field were damaged due to reservoir compaction, leading to a 40 percent abandonment rate (Sasaki et al., 2019). The integrity of wells can be undermined by a multitude of factors, as evidenced by the buckling, tension, and shear failures of wells in the North Sea's Ekofisk field, induced by compaction in the reservoir's weak chalk layer (Schwall and Denney, 1994). The financial implications of these well failures are massive, with countermeasures potentially reaching up to one billion dollars (Nagel, 2001). However, these failures and subsequent financial burdens could be preventable, or at the very least, mitigated through proactive measures.

Well monitoring serves as a cornerstone in the effective management of well integrity, with its primary objective being to diagnose the health and condition of wells, consequently enabling optimized production or operation. A wide array of integrity test methods is currently employed in the industry, each with unique capabilities and applications. These methods include neutron logging, a technique that measures porosity in the formation by detecting neutrons (Kiran et al., 2017); and noise and temperature-based indicators for fluid movement, which provide insights into the dynamics of the well's contents (Al-Hussain et al., 2015). Other techniques include magnetic flux leakage (Peng et al., 2020; Assous et al., 2021) and

ultrasonic inspections (Mohammed et al., 2019), both of which are used for casing inspections to detect defects or corrosion in the metal casing of the well. Mechanical calipers (Mohammed et al., 2019; Assous et al., 2021) measure the internal diameter of the wellbore or casing, while downhole cameras provide visual (Al-Zain et al., 2016) inspection capabilities. Cathodic protection profile surveys are also used to assess the effectiveness of corrosion control in the well (Ojeda et al., 2016).

While conventional logging operations can provide valuable information on the location of damage related to casing integrity or cement sheath conditions, there are limitations to these methods. Most notably, these conventional methods often require the suspension of well operations for the duration of the test, which could impact production. Moreover, due to the intrusive nature of these methods, they can only be implemented on a yearly basis, or in some cases, even less frequently. This infrequency might limit the timely detection of potential issues, underscoring the need for more regular and less disruptive testing methods for well monitoring.

The implementation of efficient, continuous real-time monitoring plays a crucial role in the accurate detection and correlation of well damage with specific production or intervention events (Braga et al., 2013). To proactively prevent unforeseen well failures and continuously monitor the operation of the well, it is essential to conduct real-time and distributed monitoring of well integrity. The distributed fiber optic sensing technique shows its potential for this purpose, being effective in monitoring the well's temperature in vertical wells (Sasaki et al., 2019). With the assistance of high-density distributed data and real-time data processing capabilities, gas leakage following tubing breakage can potentially be monitored by distributed temperature sensing (DTS). The efficacy of real-time DTS in detecting aberrant behavior via a modeling system has been expounded upon in previous works (Zhang et al., 2022). In addition to the temperature monitoring, distributed strain sensing (DSS) was applied to observe tubing deformation under abnormal stress conditions that may lead to tubing failure. As storage wells are subject to degradation over time, it is imperative to include deformation monitoring within the well integrity assessment process. Consequently, the stress-strain response curve, detectable via DSS, can serve as a powerful tool, offering invaluable insights for integrity evaluations.

This project developed and tested novel, noninvasive technologies designed to assess the integrity of the UGS wellbore. This innovative approach involves two technologies: distributed fiber optic sensing (DFOS) that includes distributed strain and temperature sensing (DSTS), which requires installation of downhole fibers, and the electromagnetic time domain reflectometry (EM-TDR), which eliminates the need for any downhole sensors or the opening of the wellhead; thus, completely non-invasive and non-interruptive to borehole operations. The expedited setup process and noninvasive characteristics make these technologies not only suitable for immediate diagnostic applications but also potentially viable for long-term monitoring purposes.

CHAPTER 2:
Project Approach

The main goal of this project is to explore potential methods for monitoring UGS wells, focusing on the development of DSTS and EM-TDR. This involves several laboratory tests and a field demonstration. The project is divided into two key areas based on the technology focus:

1. Developing and verifying the application of DSTS in UGS wells.
2. Developing and verifying the application of EM-TDR in UGS wells.

Following the Aliso Canyon events, most operators adopted tubing and packer configurations to meet the regulatory requirements of California Code of Regulations, Section 1726.5, ensuring two barriers in the well. These wells consist of three essential components for gas containment: casing, tubing, and packer. The unpredictable nature of damage to casing and tubing, often located deep in the well, underscores the importance of using DSTS and EM-TDR for damage location. These methods measure changes in temperature, strain or impedance profiles to identify damage.

The annulus is the open space between the casing, which maintains the borehole's geometry and integrity, and the tubing, which serves as the pathway for gas storage/retrieval. The annulus is usually filled with a mixture of water and corrosion inhibitor, with the water level maintained at a specific level and monitored using temperature readings. Fluctuations in this water level could indicate casing failure, either due to groundwater ingress or drainage of annulus water. Additionally, leakage can result in pressure changes in the annulus, detectable through temperature profile readings. These temperature tests, primarily conducted at C-FER Technologies (also referred to as C-FER in this report), will include controlled leakage experiments, which are discussed later.

Damage to casing or tubing from corrosion, internal pressure cycling, or external forces (like shear from faults) leads to detectable changes in strain, recorded at deformation locations using distributed strain sensing. The project investigates strain changes due to corrosion (simulated by grinding to reduce tube thickness), pressure cycling (using nitrogen), and external forces (via shearing and tension/compression tests).

The practical application and real-time performance of these technologies were also assessed at a field site on McDonald Island, a Pacific Gas and Electric Company (PG&E) gas storage site. This included developing installation methods during the field site installation, which is discussed in further detail later.

Distributed Fiber Optic Sensing

Technology - Distributed Fiber Optic Sensing and Fiber Optic Sensing Cable

Real-time monitoring of well integrity is crucial to prevent unexpected well failures. Distributed strain sensing using fiber optics offers an innovative solution for well integrity monitoring,

providing high-precision, real-time measurements of well deformations. In the oil and gas industry, Raman scattering-based DTS is prevalent in DFOS. However, this method is limited because it only measures temperature and requires regular calibration due to power loss along the optical fiber. Additionally, the use of multimode fiber constrains the sensing distance and spatial resolution. In contrast, Brillouin scattering based DFOS, a rising technology, simultaneously measures strain and temperature by detecting shifts in the Brillouin scattering spectrum in the frequency domain. This approach eliminates the need for regular recalibration and supports continuous, long-term use.

The Brillouin scattering system measures strain and temperature change simultaneously as shown in Equation 1. In order to distinguish between temperature and strain, two optical fibers were used: one with effective strain transfer to measure both strain and temperature, and another isolated from strain transfer to measure only temperature. By compensating for temperature using the measurements from both optical fibers, the strain profile can also be collected.

$$\Delta\nu_B = C_{\epsilon,B}\,\Delta\epsilon + C_{T,B}\,\Delta T \quad (1)$$

Where ΔV_B is the frequency shift in Brillouin backscattering spectra, $C_{\epsilon,B}$ is the strain coefficient for Brillouin backscattering, $C_{T,B}$ is the temperature coefficient for Brillouin backscattering, $\Delta\epsilon$ is the strain change, and ΔT is the temperature change. The coefficient does not change with the interrogation system. The strain coefficient is usually 500 megahertz per percent (MHz/%) and the temperature coefficient is usually 1 megahertz per degree Celsius (MHz/°C).

The project team developed a Brillouin optical time domain reflectometry (BOTDR) system to measure temperature and strain with a single unit (Figure 1). The unit is capable of taking readings from an optical fiber sensing cable that has two optical fibers inside (Figure 2). A specialized optical fiber cable, designed specifically for DSTS in UGS integrity monitoring at

Figure 1: Fiber Interrogation Unit

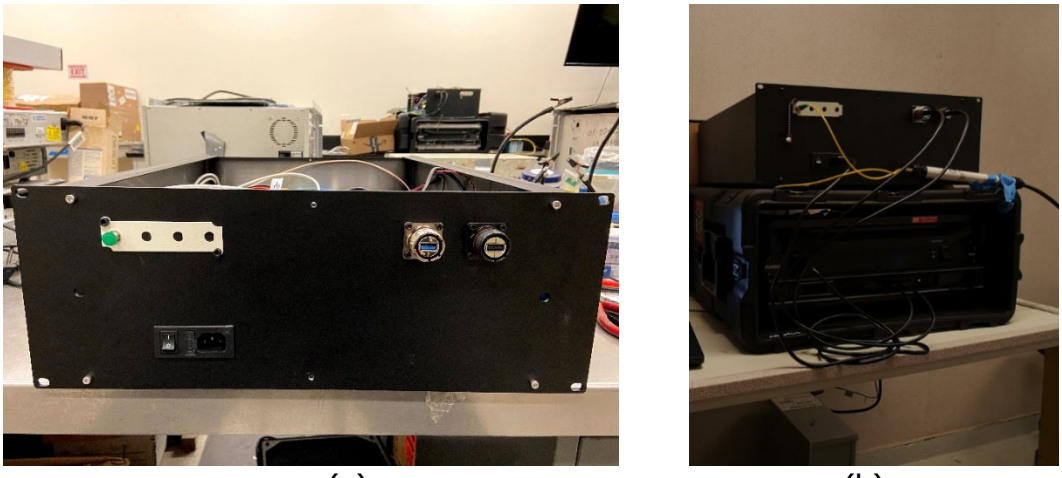

(a) (b)

(a) The front panel of the enclosure. This front panel includes FC/APC connector, power switch and USB connectors. (b) The home-made DSTS interrogator at the field demonstrations.

Source: LBNL

Figure 2: Cross-section of the Fiber Optic Cable

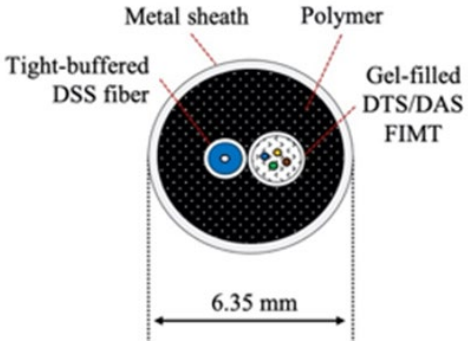

DAS = distributed acoustic sensing
Source: Sasaki et al., 2021

Lawrence Berkeley National Laboratory (LBNL) incorporates two distinct optical fiber designs. This design benefits from synergies with other borehole monitoring projects conducted also at LBNL. It features a central loose tube single-mode optical fiber and a tightly bonded single-mode optical fiber, both of which can be simultaneously interrogated for continuous readings. The central loose tube optical fiber, insulated from strain by gel with Fiber In Metal Tube (FIMT) structure, is dedicated to measuring temperature only. In contrast, the tightly bonded optical fiber is capable of measuring both temperature and strain. This dual functionality reduces installation cost and enhances monitoring efficiency and accuracy. The cable, with a diameter of 0.25 inch, is encased in a steel sheath, providing robust protection for the optical fibers in downhole applications. For DSS, the cable includes a single-mode optical fiber, while the DTS component of the cable houses two single-mode optical fibers along with two multi-mode optical fibers. The configuration of this cable design is illustrated in Figure 3.

Figure 3: Pressure – Strain Response Tests

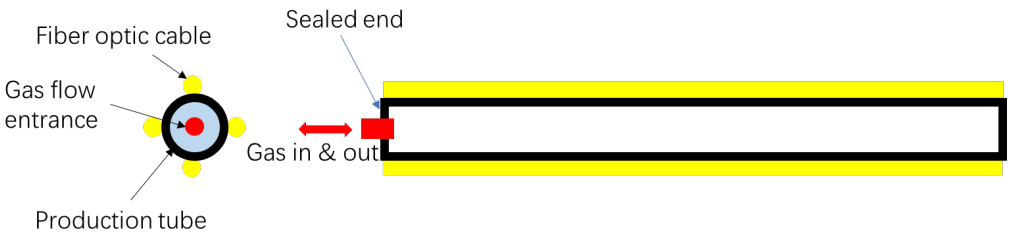

Source: LBNL

Laboratory Feasibility Tests:

The primary objective of conducting laboratory feasibility tests was to assess the viability of using DFOS for monitoring the integrity of UGS wells. These tests were specifically designed to evaluate the effectiveness of distributed fiber optic strain and temperature sensing in detecting and monitoring potential leakages in boreholes of UGS wells. Table 1 provides details the specific tests carried out.

Table 1: Lab Tests Conducted by LBL and UCB

Test	Test Purpose	Test Facilities	Locations	Target
Pressure test	To test the tubing strain under pressure	Pressure	Richmond field station	Tubing
Pressure test with damage	To test the strain response when the tubing has been damaged compared to previous test	Pressure	Richmond field station	Tubing
Shearing test	To test the strain response when casing shears and the strain transfers to tubing	External force shearing test	Richmond field station	Casing and potential tubing deformation
Tension and compression test	To test the strain on casing under tension and compression	External pulling and compres-sing force	Richmond field station	Behind casing and casing
C-FER test	To double blind test the temperature variation during the simulated leakage events and the strain development during the pressure cycle	Temperature leakage events and pressure cycles	C-FER Technologies, Canada	Tubing

Source: LBNL

Test 1 and Test 2: Pressure Tests

For pressure testing, both ends of a 10-foot production tubing were sealed, as shown in Figure 3. To simulate pressure cycles within the tubing, nitrogen gas was injected, varying the pressure from 0 pounds per square inch (psi) to 2200 psi. Four optical fiber cables were affixed to each of the tubing's four sides, enabling the recording of strain responses when the tubing was subjected to internal pressurization.

The test procedure then progressed to a simulated damage scenario. This involved repeating pressure changes inside the tubing after manually creating a simulated corrosion effect. A 2-inch square section of the tubing was thinned to half its original thickness, representing a corrosion-thinned layer (Figure 4). This alteration allowed for the assessment of the system's response to structural weakening, mimicking real-world corrosion effects.

Figure 4: Pressure – Strain Response Tests for Compromised Tubing Under Thinned Conditions

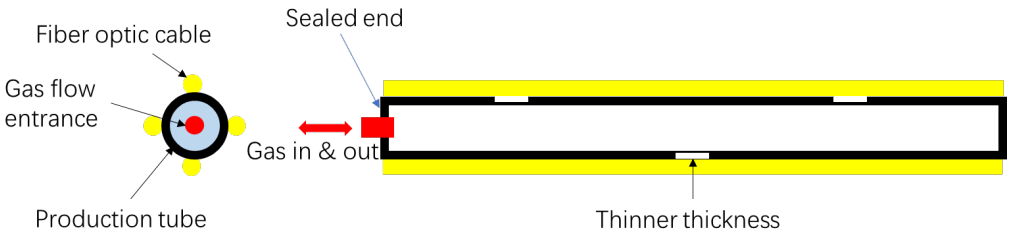

Source: LBNL

Test 3: Shearing Test

This test was designed to simulate the impact of external forces, such as fault movement, on a well configured casing and tubing. Optical fibers were installed along the top, left, and right sides of both the casing and tubing, each measuring 10 feet in length. The casing and tubing were secured to two steel plates using eight steel clamps. To simulate fault movement, the right platform was incrementally moved a total of 19 inches in 0.5-inch steps, mimicking a fault movement at a 60 degree angle. Alongside the DFOS strain measurements, strain gauges and displacement sensors were also installed for verification purposes. During the test, the tubing, suspended within the casing, was subject to shearing forces as the casing deformed significantly due to the movement of the plate.

Figure 5: Schematic of the Setup for the Shearing Test

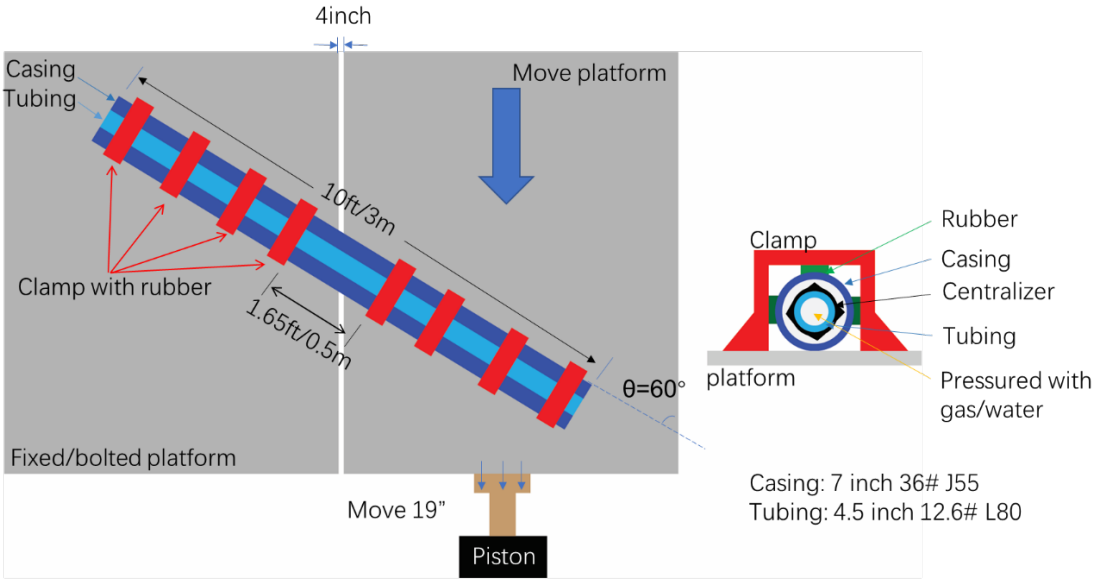

Source: LBNL

Test 4: Tension and Compression Test

In this test, the optical fiber cable was simulated to be installed behind the casing with cement and the casing was under the tension and compression external load at two sides. The test sample (Figure 6 and Figure 7) consisted of two A36 steel Schedule 40 pipes and the grouting material in between. The outer pipe, which was used to simulate the rock layer, has an outer diameter of 12 inches and a wall thickness of 0.4 inches. The inner pipe, which simulates the casing in the UGS well, has an outer diameter of 8.625 inches and a wall thickness of 0.325 inches. Both pipes were 120 inches long. In the center, a 2-inch-thick flange with an outer diameter of 24 inches was weld to the outer pipe. There were six steel rods connecting the center flange and the bottom steel plate and the forces provided from the load cell could be transmitted through these rods. The grouting material poured in between the two pipes was a mixture of Portland cement and water. Fiber optic cables were installed at the four sides between the two steel pipes and were held by the cured cement, shown in the following figure. Four kinds of fiber optic cables were tested in this experiment including: a) 0.25-inch steel jacked cable; b) 0.25-inch nylon jacked cable; c) a tight buffered cable; and d) a loose

tube cable. Fiber optic cables of the same type at different locations were spliced into one loop, forming four channels for reading using a high-resolution fiber optic strain sensing system.

Figure 6: Schematic of the Setup for Tension and Compression Test (top view)

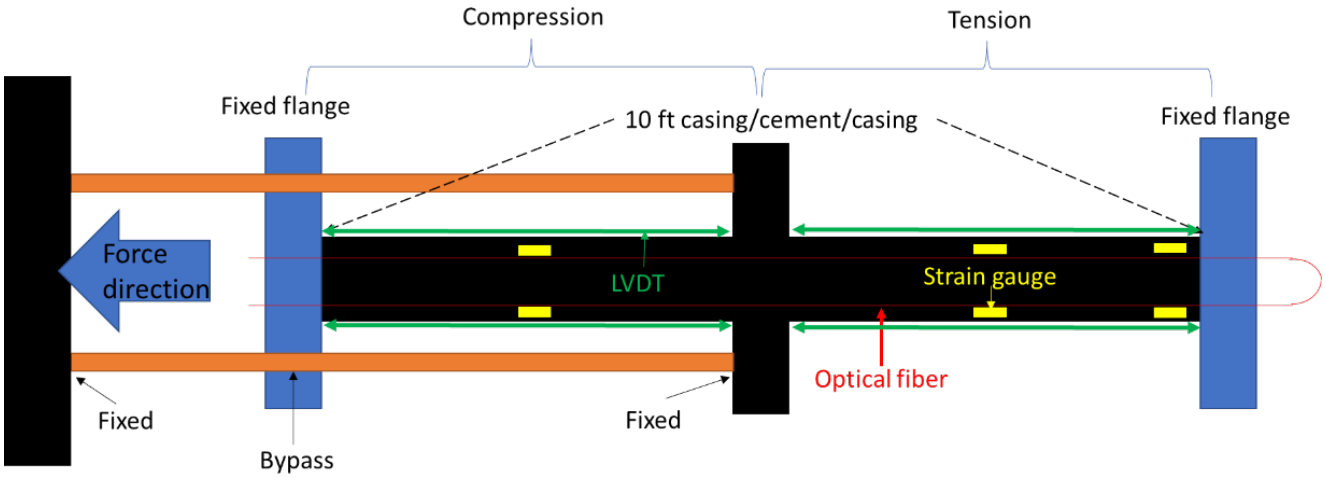

Source: LBNL

Figure 7: Schematic of the Tension and Compression Test (cross-section view)

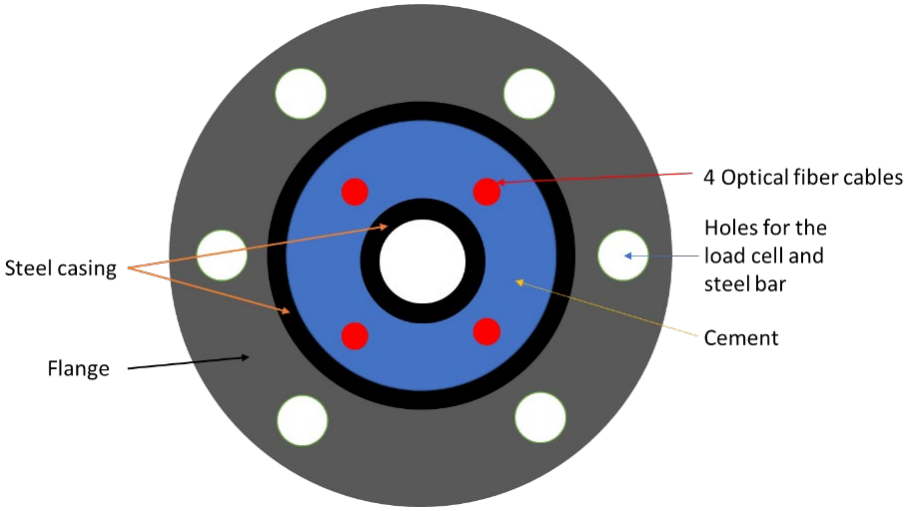

Source: LBNL

Test 5: C-FER Test

This test focused on the verification of using DFOS for leakage detection and strain monitoring during the pressure cycles in a mock well configuration. The experimental investigation was executed at the C-FER laboratory (Edmonton, Canada), using a test well comprised of a 4.5-inch tubing string and an 8.625-inch casing string to replicate the completion of an UGS well. The schematic representation of the test well setup is illustrated in Figure 8. A section of 8.625-inch production casing, measuring approximately 12 feet in length, was cemented within a 10.625-inch casing, thus simulating a borehole.

The tubing was installed concentrically within the casing, and the annulus between the casing and the tubing was filled with water and sealed at both ends. This mirrors the standard UGS well completion process where completion fluid occupies the annular space between the casing and the tubing. The optical fiber cable was securely fastened to the external surface of the tubing using centralizers and clamps, which is the same as the field demonstration. The installed fiber optic cable is a 0.25-inch diameter, enveloped within a steel sheath, which houses two distinct optical fiber tubes designated for DSS and DTS, respectively. The DSS tube contains a single-mode optical fiber, while the DTS tube accommodates two single-mode optical fibers and two multi-mode optical fibers. The experiments were conducted to simulate two distinct processes:

1. A temperature variation test simulating possible changes during gas injection, or withdrawal, or leakage scenarios. Variations in temperature that could be triggered by liquid and gas leaks at assorted depths, were simulated by deploying a water spray nozzle into the tubing string at pre-determined depths, and subsequently injecting either hot or cold water.
2. An accelerated cyclic pressure test in the tubing, devised to mimic the cyclical process of gas injection and withdrawal over time. This test was performed with the intention of evaluating the robustness of the fiber attachment system and to simulate potential fatigue and deformation effects on the tubing due to recurring loads, which encompassed 500 pressure cycles, conducted over a duration of eight hours.

Figure 8: Test Well Setup

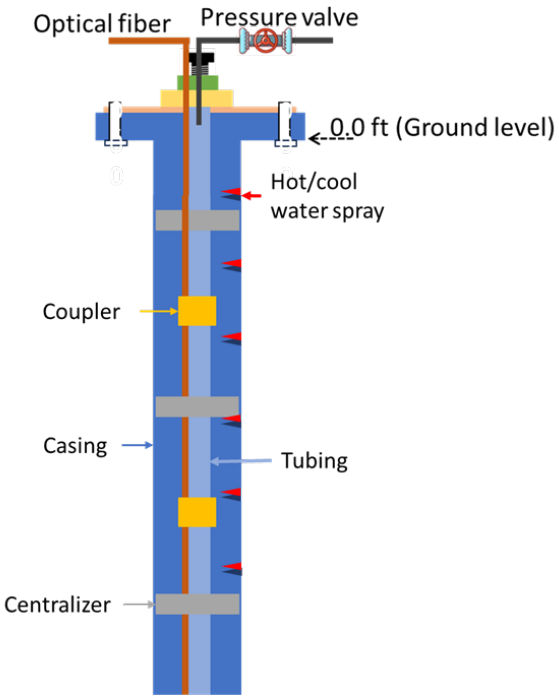

The tubing was installed at the center of the casing with two couplers and three centralizers. Water sprayers were installed in the annulus to spray hot and cool water to the tubing at certain depths.

Source: LBNL

Field Demonstration

The DFOS technology was demonstrated at a field site located at McDonald Island, California with the collaboration of Schlumberger who installed the fiber sensors. The developed BOTDR system was used to measure temperature and strain with an updating rate of 15 minutes for a 5,500-foot fiber optic cable installed along with the 4.5-inch outer diameter tubing. The cables were installed and secured above the packer, below the wellhead, and clamped to the tubing using a clamp (Figure 9a) at each junction between two tubing strings. To prevent the optical fiber cable from being squeezed between the tubing and casing during installation, centralizers (Figure 9b) were used in the middle of each tubing string.

Figure 9: Drawings of the Coupler and Centralizer Used in the Field Demonstration

(a)

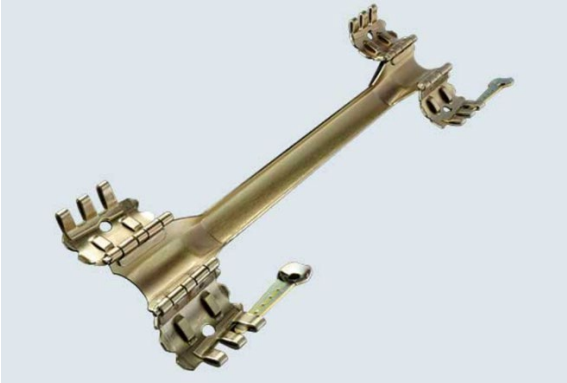

(b)

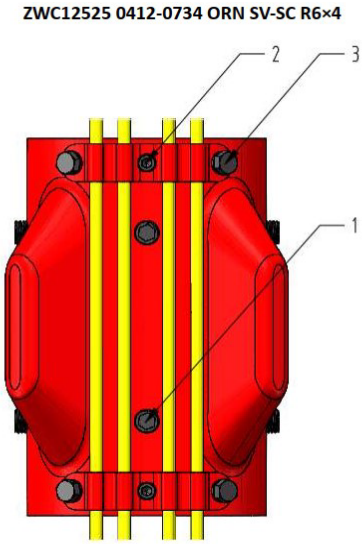

Item	Description	Qty	Specification	Wrench Specification
1	Set Screw	8	1/2-13UNC	Allen Wrench 1/4
2	Inner Hexagon screw	1	1/4-20UNC	Allen Wrench 3/16
3	Outer Hexagonal Screw	2	1/4-20UNC	Wrench 7/16

Source: Slingco and Schlumberger

The optical fiber cables were spliced to the surface cable and the splices were protected in a junction box that was fixed to a concrete post located beside the wellhead. Figure 10 shows four photos taken at the field site. The interrogator took readings during three periods:

- Pressurization reading: immediately following the optical fiber cable installation, during the pressurization test, for a few hours. Each reading was taken at each pressurization stage inside the tubing or in the annulus.
- Continuous reading: for seven months from November 2021 to June 2022. Readings were taken every 15 minutes for strain and temperature from November 15, 2021, to June 8, 2022. Channel 1 of the interrogator was connected to the strain optical fiber while Channel 2 was connected to the temperature optical fiber. Data was sent to the

cloud in real time and can be further processed at the cloud edge. There were multiple periods where data collection was not possible due to power supply instability.

- Temperature/noise logging test in November 2022. After the ground construction was complete, the well was investigated by temperature/noise logging. DFOS temperature data was collected at same time and compared to the temperature logging result.

Figure 10: Photos Taken at the Field Demonstration Site

Top left: Optical fiber cable is hanged by a sheave to help installation. Top right: Optical fiber cables are bonded by hose clamps at the bottom of the well above the packer. Bottom left: Optical fiber cables passed through the well head. Bottom right: Optical fiber cables and splicing were secured at the junction near the wellhead.

Source: LBNL

EM-TDR

Background

Time-domain reflectometry has been used for locating faults on conductive cables or pipelines (Furse et al., 2009; Amir et al., 2010) as well as for measuring soil water content and bulk soil electrical conductivity (Topp and Davis, 1985; Herkelrath et al., 1991; Heimovaara, 1993) by sending high-frequency electromagnetic pulses into the medium under investigation and recording the reflected signals. Similar to seismic guided waves (Wang et al., 2016), TDR signals propagate inside the conductive medium, which is under examination, and reflect at the interfaces with impedance changes (such as joints, faults, terminations). The travel time and the waveforms of the reflections (for example, shape, polarity, and magnitude) relate to the distances and the dielectric characteristics of the faults (for example, the size of the damage), respectively. The proofing of the concept of using the EM-TDR method in the wellbore scenario was studied previously via numerical sensitivity test, laboratory test, as well as field test (Wang and Wu, 2020). In this project, EM-TDR was optimized for more realistic settings.

In this project, both double-blind laboratory tests and field tests were conducted to verify the technology. The double-blind laboratory tests were collaborated with C-FER Technologies of Canada and used their deep well simulator facility. The field tests were conducted in collaboration with PG&E of California and at their McDonald Island gas storage facility. Additionally, laboratory tests were conducted in the laboratory for further technical development and validation. These results are summarized in the subsections below.

Double-blind Laboratory Tests at C-FER Deep Well Simulator

C-FER Technologies, a non-profit subsidiary of Alberta Innovates in Canada, possesses specialized knowledge in extensive testing facilities. The Deep Well Simulator at C-FER was purposefully designed to execute tests that replicate realistic scenarios while upholding a controlled environment for subsequent assessment and calibration of the EM-TDR technology. The experimentation involved three varying sizes of casing strings: a 4.5-inch diameter, a 5.5-inch diameter, and a 7-inch diameter. These casing strings, between 80 and 90 feet in length, were suspended from the ground level supporting plate into the Deep Well Simulator. To ensure electrical separation between the wells, an insolation layer was positioned between the casing strings and the hanging plate.

To replicate realistic conditions and assess the precision and sensitivity of the EM-TDR method, complex and diverse metal loss characteristics were introduced onto the casings. These characteristics encompass natural corrosion, machined pinholes, pitting, circumferential grooving, clusters of pitting, axial grooving, circumferential cutting, and manually crafted irregular-shaped features. Specifically designed for wellbore integrity monitoring, corrosion events precede bursting. For such purpose, all introduced features maintain a remaining burst strength of approximately 3,000 psi, aligning closely with the typical maximum operating pressure of underground gas storage wells. To evaluate the potential impact of cement on the EM-TDR detection performance, the bottom section of the 4.5-inch casing string was

cemented. A schematic diagram of the Deep Well Simulator setup, including the feature configuration unknown prior to the EM-TDR interpretation, is shown in Figure 11.

In this double-blind test, the LBNL research team remained unaware of both the feature configurations and their distribution until the completion of final EM-TDR interpretation, including measurements, data processing, and overall analysis. Prior to the final interpretation

Figure 11: EM-TDR Double-Blind Laboratory Test Setup

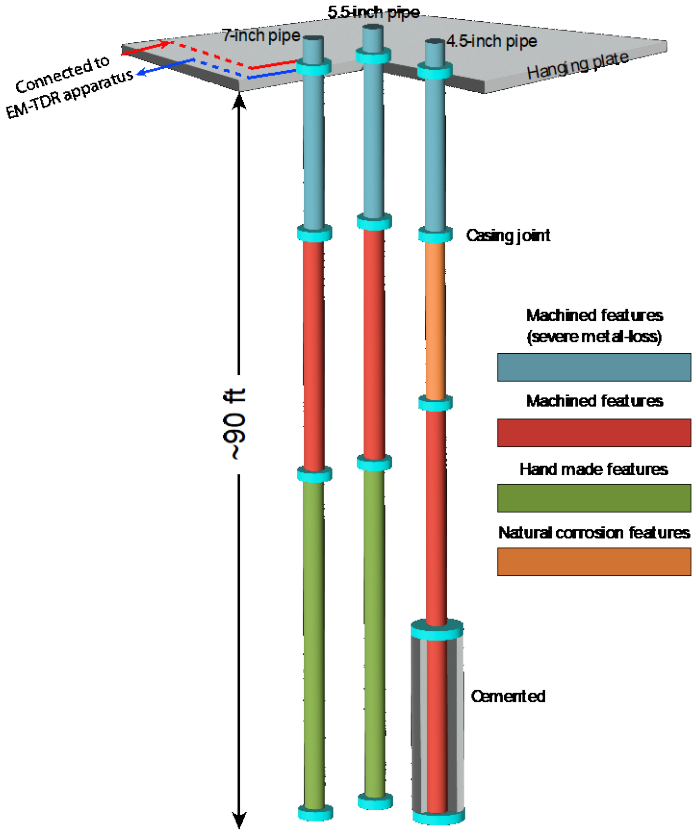

Figure 11. Schematic representation of the EM-TDR double-blind test conducted at the Deep Well Simulator, based on the ground truth revealed after completing measurements and interpretation. The Deep Well Simulator has a total depth of 150 feet. Pipes were suspended from the surface hanging plate, not reaching the bottom of the Deep Well Simulator. The pipe length ranges from 80 to 90 feet. Pipe section numbers, lengths, and feature configurations were undisclosed prior to measurements and interpretation. Casing joints are highlighted in cyan. The EM-TDR apparatus was connected at the top of the pipe under testing, positioned below the first casing joint. The sending and receiving of EM waves are denoted by red and blue arrows, respectively.

Source: LBNL

delivery, the only information available regarding the casing strings pertained solely to the diameter of the casing, the number of sections, and the length of each casing string.

The tests were conducted remotely from March 26 to March 31, 2022. Both the electromagnetic source and the oscilloscope were connected to the wellhead via coaxial cable. To capture potential small-size features and address attenuation challenges within each casing string, measurements were undertaken across a diverse range of frequencies. The frequency spectrum initiated at 150 MHz and extended up to the highest frequency of 2 gigahertz (GHz).

To enhance the signal-to-noise ratio and suppress the random electronic noise, individual measurements were taken 300 times then combined and counted as a single measurement.

Blind Field Test at PG&E McDonald's Island Gas Storage Site

PG&E is a utility company based in San Francisco, providing electric and gas services throughout Northern and Central California. The blind field test was conducted at PG&E's McDonald's Island gas storage site, Turner West. This is the same location where the fiber technology described above was tested, but the EM-TDR tests were conducted on different wellheads. Figure 12 illustrates the aerial view of the wellbore's location. The selected well for testing is decommissioned, retaining only the surface casing. This specific wellbore was chosen due to its lack of electrical connectivity with other wellbores and gas processing facilities through pipelines.

Figure 12: Location of the EM-TDR Blind Field Test

The EM-TDR blind field test is at the PG&E McDonald Island facility. The red circle indicated the wellbore under test.

Source: LBNL, Google Maps

The wellhead of the wellbore under test was still not open (Figure 13a). The electromagnetic source and receiver (the scope of the oscilloscope) were connected to the gas pressure valve on the wellhead (Figure 13b). Because the other wells of the facility were still in operation, one of the immediate challenges was the high-frequency range signal (2 GHz) was closely aligned with the radio communication frequency employed in the operational wellheads of the facility. This alignment posed a potential risk of introducing coherence noise to the EM-TDR measurements (Figure 13c), particularly given the concurrent operation of other facility wells.

Figure 13: Photos Taken at the Field Test Wellhead of the Tested Wellbore

(a) The wellhead of the tested wellbore. (b) The pressure valve on the wellhead was used for sending and receiving electromagnetic waves. (c) The communication antenna on the wellhead.

Source: LBNL

CHAPTER 3:
Results

Distributed Fiber Optic Sensing

Laboratory Test

The laboratory test result proved the potential of using DFOS for UGS well integrity monitoring. The tests results are summarized in the following subsections.

Pressure Test

The strain results from optical fiber sensing show a nearly linear relationship between the internal pressure and the tube strain. This suggests that changes in pressure during actual operations inside the well could be monitored by analyzing the strain distribution along the tube. In cases of damage or corrosion on the tube, the strain profile can pinpoint the affected areas, as demonstrated in Figure 14a at Location 1 and Location 2, which exhibit a microstrain difference of approximately 50 to 60 compared to other locations. These findings underscore the potential of DFOS as a valuable technology for monitoring oil and gas wells, particularly for detecting corrosion in the inner tubing or outer casing. Traditional sensors are limited to providing information about potential corrosion near their installation sites, whereas distributed optical fiber allows for analysis at any position along the well.

However, achieving accurate monitoring results requires specific considerations in cable layout. To effectively capture temperature changes resulting from pressure variations, the temperature-sensitive fiber must be positioned closely against the tubing wall and securely attached to ensure consistent contact. Given that potential corrosion areas might be very small, increasing the number of cables in the circumferential direction would enhance the detection of these areas.

Figure 14: Measurement of Strain Profiles and Weakened Tubing Photo

(a) (b)

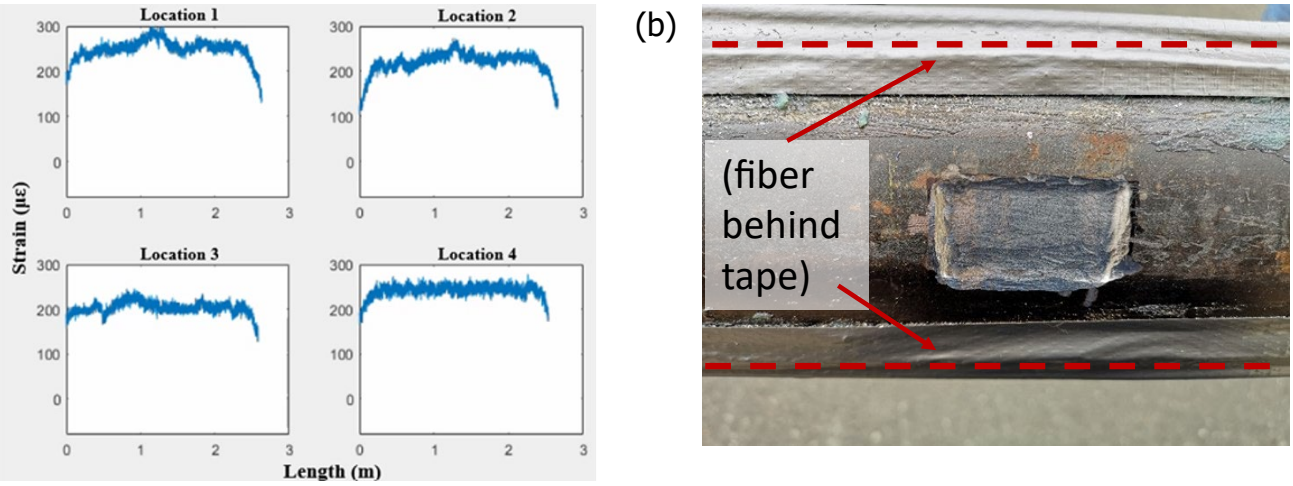

(a) The measurement of the strain profile at 4 sides of the tubing when the tubing was pressurized to 2200 psi. (b) The ground sections in the middle of the steel tube. The optical fiber Location 1 and Location 2 were at the two sides of the ground section, which was covered by the silver color duct tape.

Source: LBNL

Shearing Test

The results reveal the strain profile of the casing when it is subjected to external shearing forces, such as those caused by fault movement. The strain profile aligns with the readings from the strain gauge, demonstrating the reliability of fiber optic strain sensing. Notably, the fiber optic method offers significantly more data points compared to the strain gauge, enabling precise localization of damage. During the event where the platform shifted by 19 inches, the casing bent and made contact with the center tubing. This contact transferred strain to the tubing when the platform displacement reached 17 inches. This indicates that in a double layer UGS well, tubing deformation is likely if there is a fault movement of about 17 inches, as shown in Figure 15. Fortunately, the potential for such deformation can be monitored in real-time using DFOS strain sensing technology (Figure 16). This early detection is crucial, as it allows for intervention before the deformation escalates to a breakage or leakage event.

Figure 15: Photos of the Shearing Test and the Strain Measured by DFOS and Strain Gauges

(a)

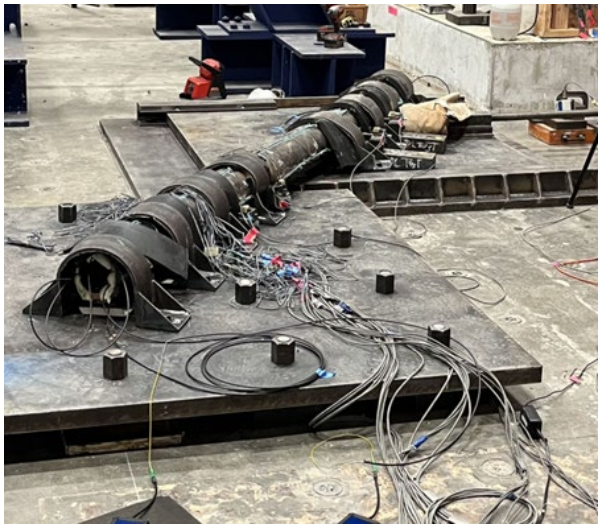

(b)

(c)

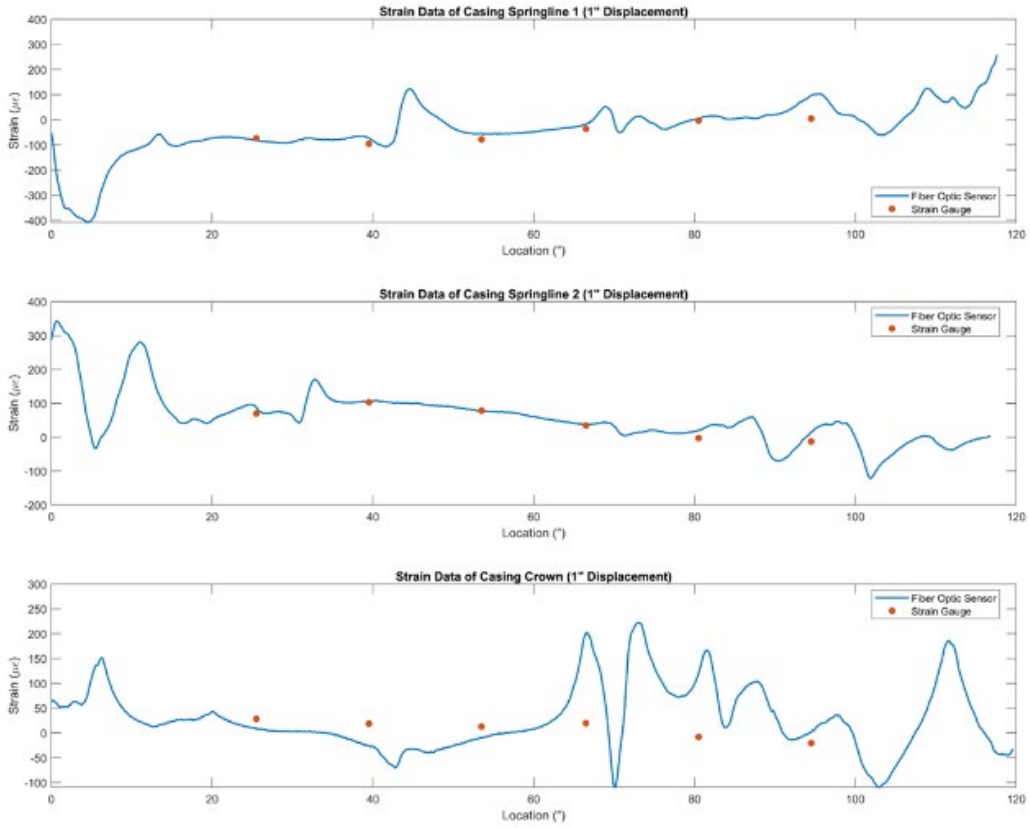
Strain Data of Casing Springline 1 (1" Displacement)
Strain (με)
Location (°)
Fiber Optic Sensor
Strain Gauge
Strain Data of Casing Springline 2 (1" Displacement)
Strain (με)
Location (°)
Fiber Optic Sensor
Strain Gauge
Strain Data of Casing Crown (1" Displacement)
Strain (με)
Location (°)
Fiber Optic Sensor
Strain Gauge

(d)

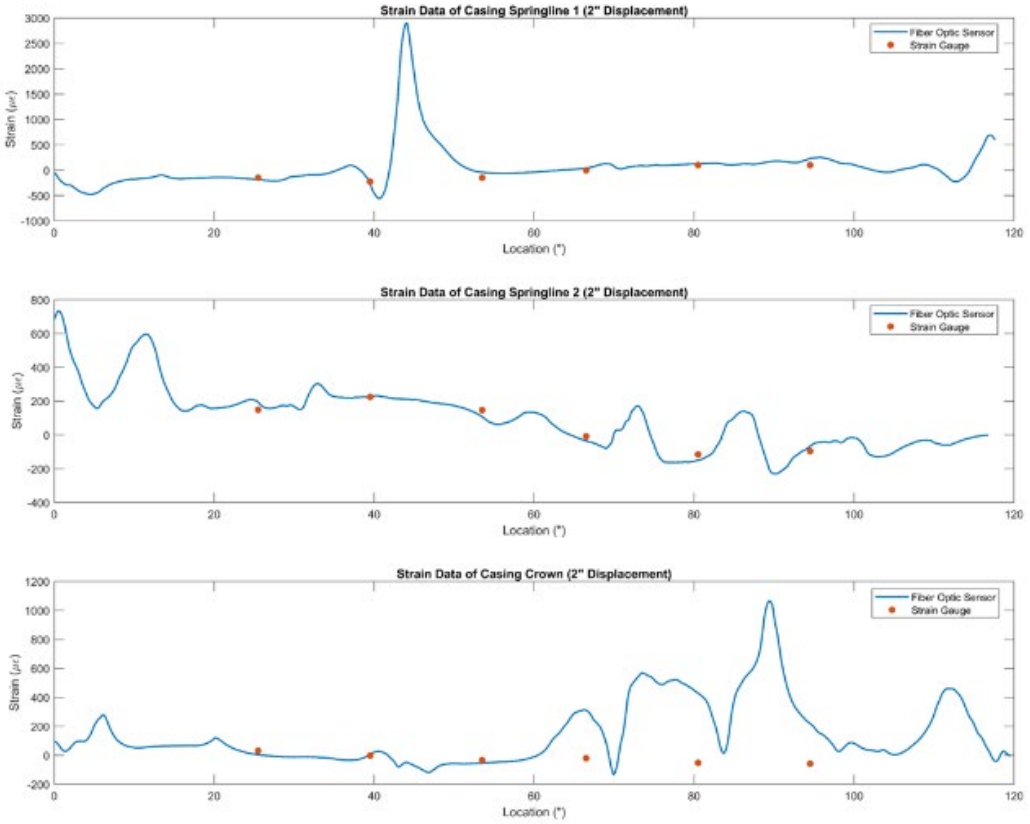
Strain Data of Casing Springline 1 (2" Displacement)
Strain (με)
Location (°)
Fiber Optic Sensor
Strain Gauge
Strain Data of Casing Springline 2 (2" Displacement)
Strain (με)
Location (°)
Fiber Optic Sensor
Strain Gauge
Strain Data of Casing Crown (2" Displacement)
Strain (με)
Location (°)
Fiber Optic Sensor
Strain Gauge

(e)

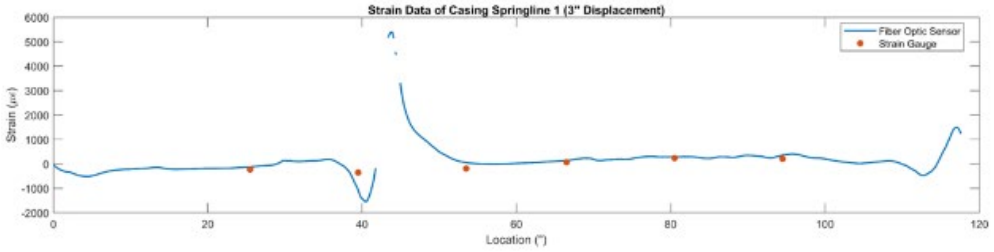

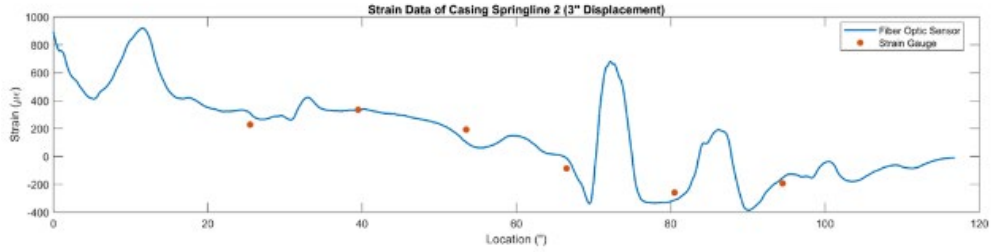

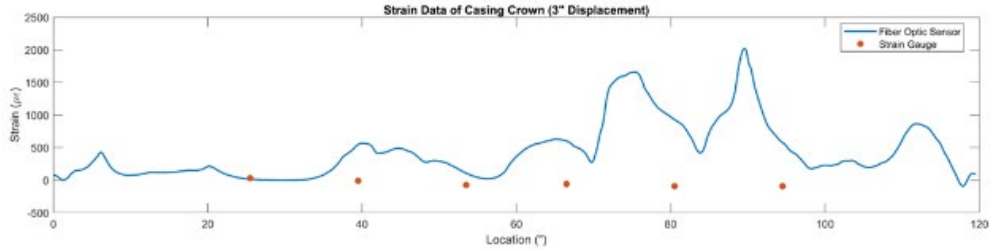

(f)

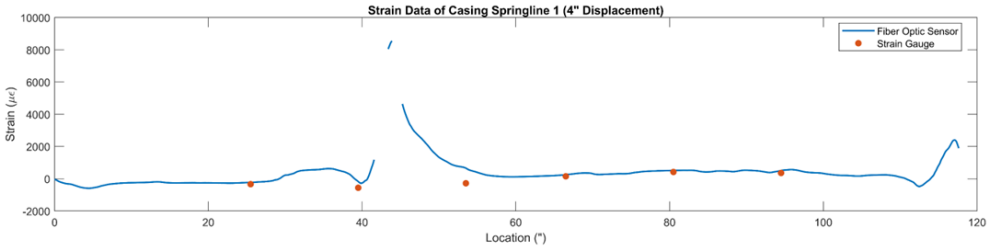

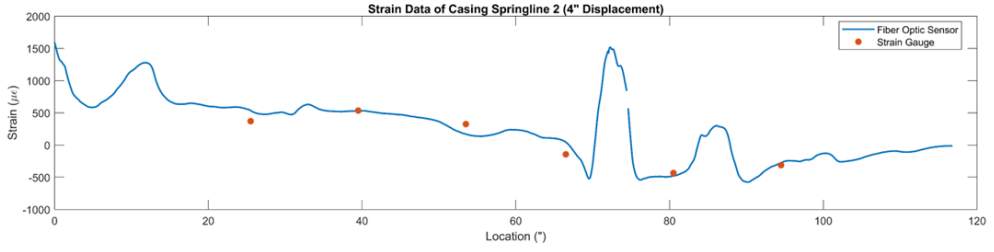

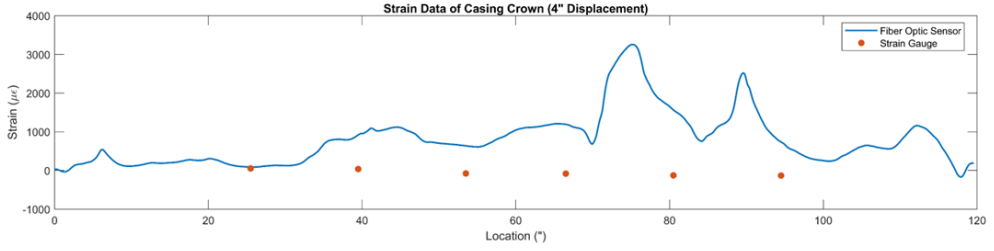

(a) Photo of the set up before the shearing test. (b) Photo of the shearing test during the shearing test. (c-f) The strain profile reading (blue line) and the strain gauge reading (red dots) when the displacement is 1, 2, 3, and 4 inches. In each displacement plot, 3 strain profile and strain gauge readings were shown for the location of left, right and crown of the casing.

Source: LBNL

Figure 16: Strain Profile on the Tubing which is Centralized inside the Casing

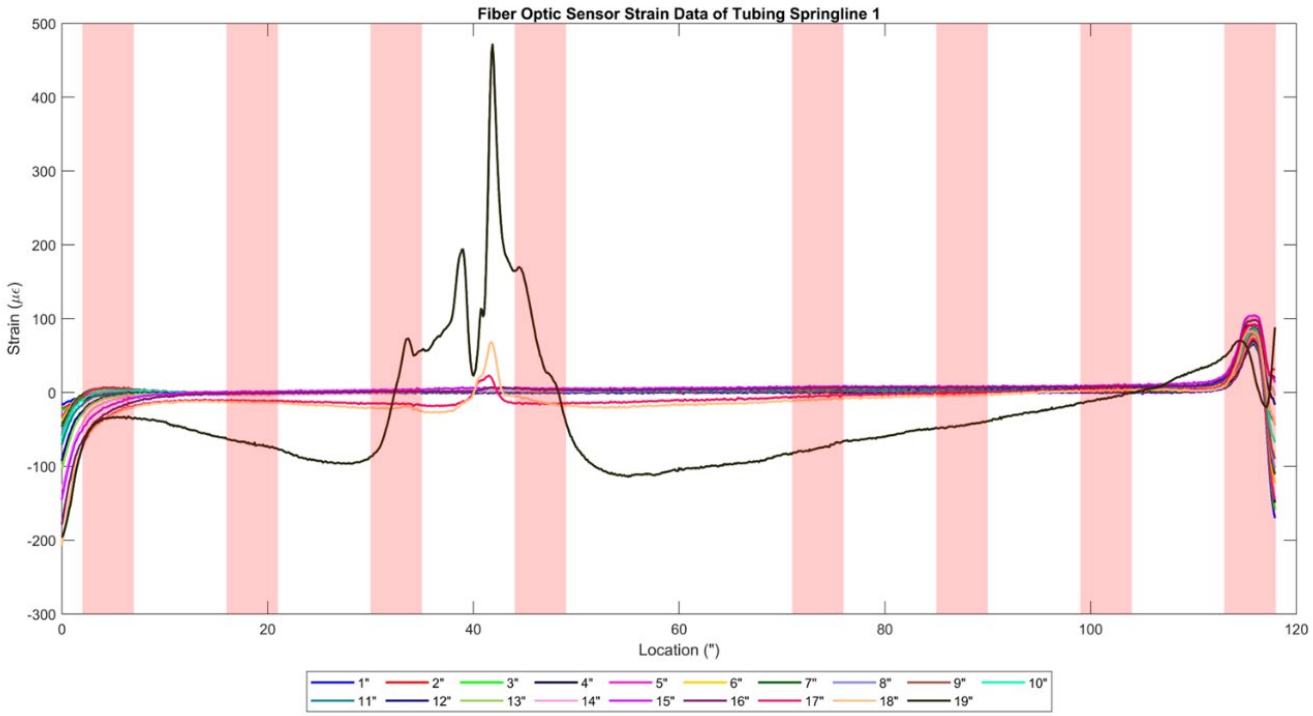

Source: LBNL

Tension and Compression Test

In new UGS wells, the optical fiber cable can be installed behind the casing to provide a deformation profile in case of casing damage. Test results indicate that the right side of the casing experiences tension, while the left side undergoes compression, as expected. This tension and compression increase with rising external load. Figure 17 illustrates the load on one side of the casing at external loads of 440 kilonewton (kN), 610 kN, 825 kN, and 1,086 kN. The optical fiber profiles demonstrate their capability to detect strain at the interface between the tension and compression sections.

During each stage, the strain readings from the tight buffer cable optical fiber closely matched those from the strain gauge. However, the other three optical fiber cables, particularly the loose tube telecom cable, did not record the same strain values, rendering them unsuitable for strain measurement. Despite its dominance in the current DFOS market and widespread use in oil and gas field applications, the loose tube telecom cable is primarily designed for temperature monitoring, not for strain or deformation monitoring. Therefore, for future UGS well strain monitoring, the tight buffer cable should be the preferred choice.

The variation in strain across different distances reflects the load differences at each cement level when pulled vertically. This information is useful for assessing the installation quality of the casing system in UGS wells.

Figure 17: Example of the Result in the Tension and Compression Test Showing the Strain Profiles Measured by the Four Optical Fiber Cables at Four External Loadings

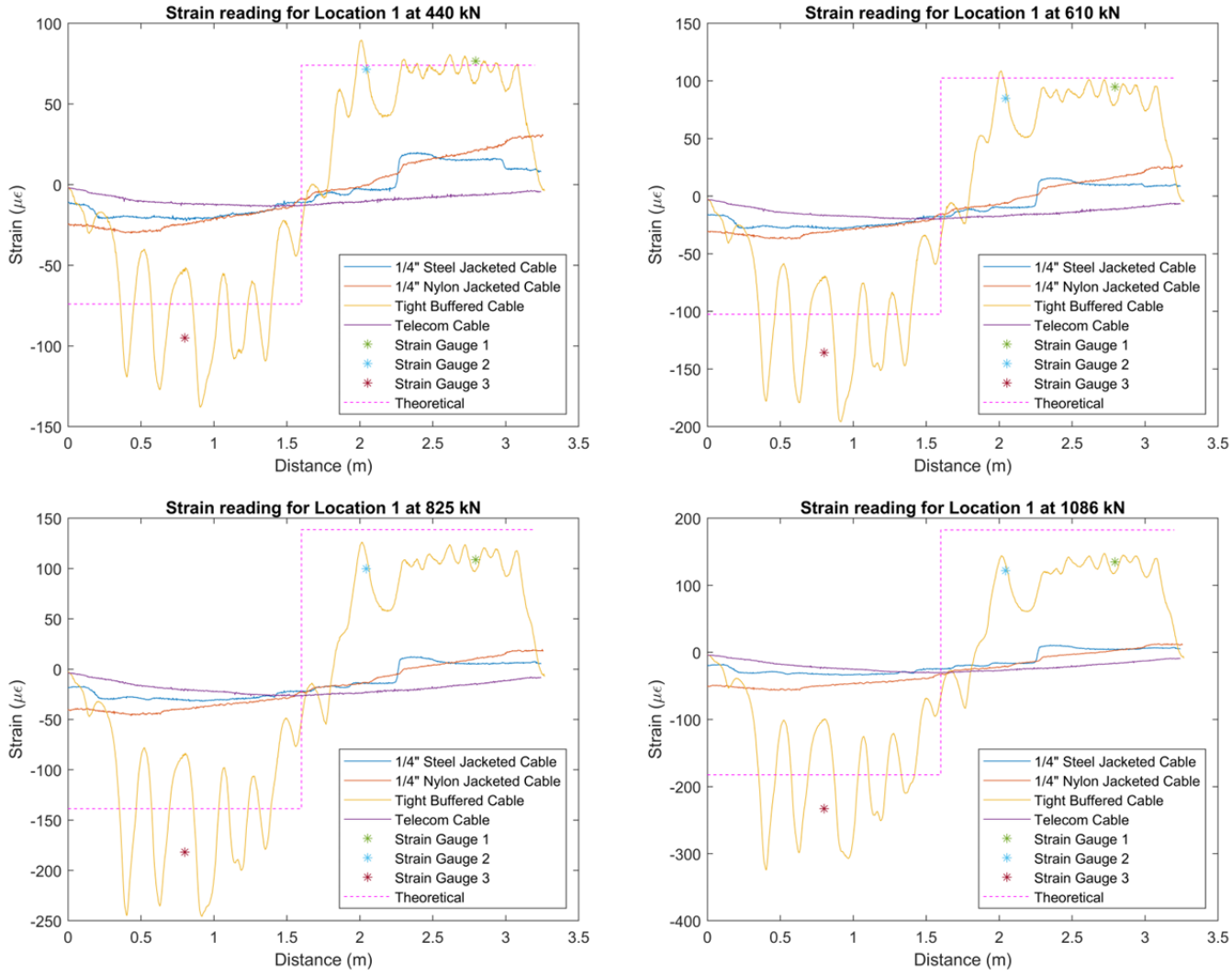

Source: LBNL

C-FER Test

The distributed fiber optic sensing system was able to successfully capture temperature profiles at all depths, using a refresh rate of 0.5 Hz, as demonstrated in Figure 18. These profiles serve to illustrate the temporal variations in temperature as a function of depth, represented on the vertical axis, throughout the entire duration of the test, denoted on the horizontal axis.

As the tubing underwent successive hot- or cold-water sprays, progressing in a bottom-to-top manner, the temperature profile effectively traced these thermal changes and precisely localized each thermal event. Manifested as a red coloration on the graph, hot water spray events indicated a rise in temperature, which rapidly propagated downward to the tubing base as the sprayed water flowed downward by gravity. This thermal event was then followed by the application of a cold-water spray, resulting in a reduction in temperature.

The waterfall chart effectively demonstrates that temperature profiles gathered by DTS can serve as a robust method to identify and localize leak events when they induce temperature changes.

Figure 18: Temperature Profile during the 12 Temperature Leakage Events

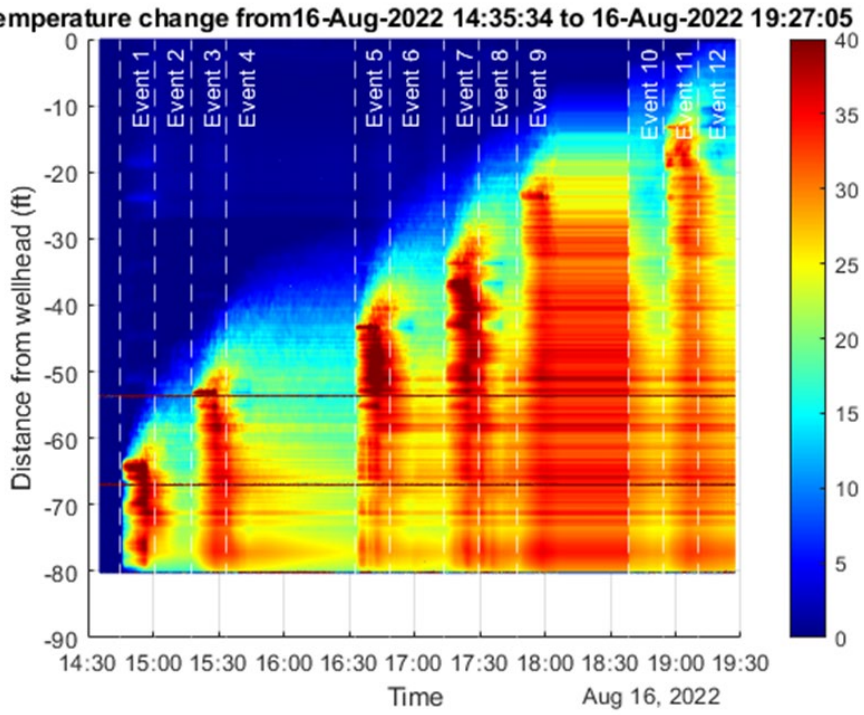

Source: LBNL

During the pressure cycling tests, after the 500th pressure cycle test, a subsequent visual inspection of the installed optical fiber revealed no apparent structural impairment or degradation of the clamps or centralizers; thereby, implying that the fiber optic cable maintained its relative positioning to the tubing without any discernible slippage.

Since the optical fiber senses both temperature and strain simultaneously, it is necessary to remove the effects of thermal changes. Therefore, the strain measurements (Figure 19a) are obtained after compensating for the influence of temperature. Tensile strain is denoted in red, and compressive strain is represented in blue; dashed lines indicate the positions of the centralizers and clamps. The strain measurements are relative changes to the state just prior to the commencement of the test. At the onset of the test, strain readings were virtually zero during the initial pressure cycles, indicating no observable effects transmitted to the DSS fiber. However, strain began to elevate at certain points, particularly between the 1st and 3rd centralizer. As the pressure cycles progressed, a compressive zone formed between the 1st and 2nd clamp, and a tension zone emerged between the 2nd clamp and 3rd centralizer. Figure 19b shows detailed strain readings for a specific section of the tubing, distinctly depicting strain variation under the cyclic pressure. Around the 35.5-foot mark, the boundary of the compression zone extended upward over time (hours 19:00 to 19:45), ultimately reaching a steady state near the 30.5-foot mark. Although strain was manifested in most of

the tubing sections, the maximum strain level remained comparatively modest (approximately 50 microstrain for both tension and compression).

Figure 19: Strain Measurements during the Pressure Cyclic Loading

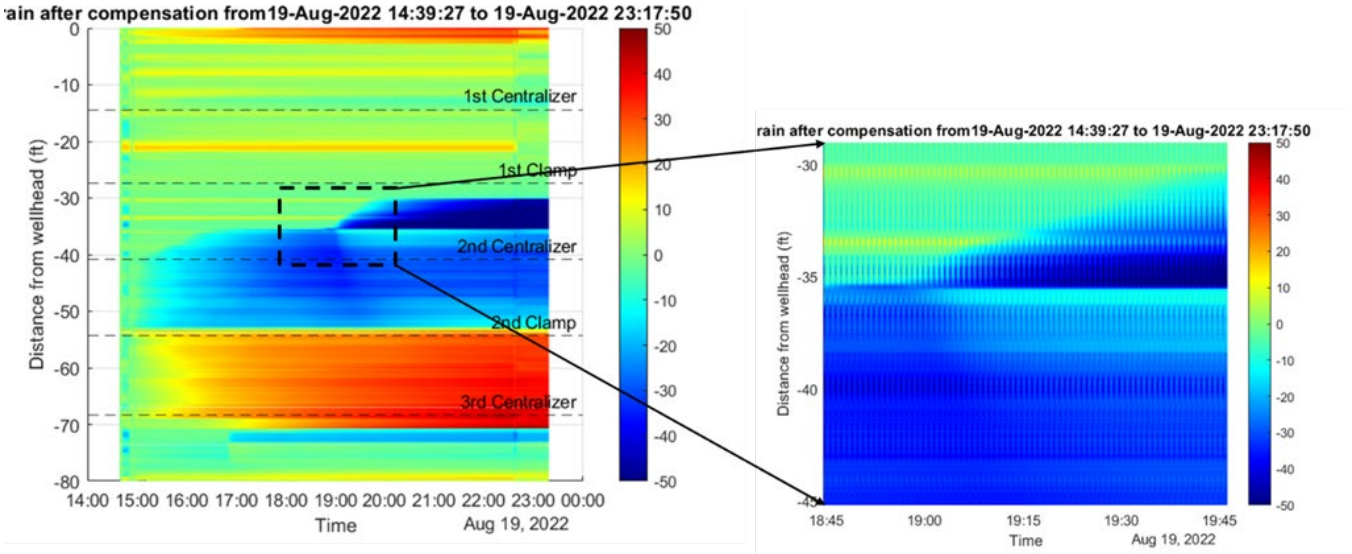

(a) (b)

(a) The strain measurement by the distributed fiber optical strain sensing. Vertical shows the depth and horizontal shows the time in this test. Color bar shows the strain value in microstrain. Red shows tension and blue shows compression. The dash square of the readings was magnified to show the details of the pressure cycle in (b). The strain is referenced to the beginning of the test.

Source: LBNL

To examine potential tubing deformation during the pressure cycles, strain was integrated from the top (as reference point) to the bottom of the well, as shown in Equation 2, and displayed the results in Figure 20.

$$displacement = \int_{top}^{bottom} \varepsilon(z)dz \quad (2)$$

Figure 20a implies that the tubing may have undergone a slight buckling phenomenon, primarily situated between the 1st clamp and the 3rd centralizer, with the deformation being notably concentrated between the 2nd and 3rd centralizer, reaching a peak at the 2nd clamp. To contrast, Figure 20b, which shows the displacement after the pressure cycle test, did not have displacement between the 2nd and 3rd centralizer. This deformation during the pressure cycle was minimal, amounting to less than 0.01 inch over an 80-foot length of tubing and non-detectable to visual inspections. The buckling phenomenon is likely a result of the tubing's end being firmly anchored at the bottom, limiting the tubing's ability to adjust its length in response to pressure cycles during the tests. This immovable end obstructed the expansion or contraction, which could lead to buckling, a common occurrence in tubing situated within a borehole, particularly in the presence of packers (Lubinski and Althouse, 1962).

Figure 20: Integrated Displacement Profiles during the Pressure Cyclic Loading

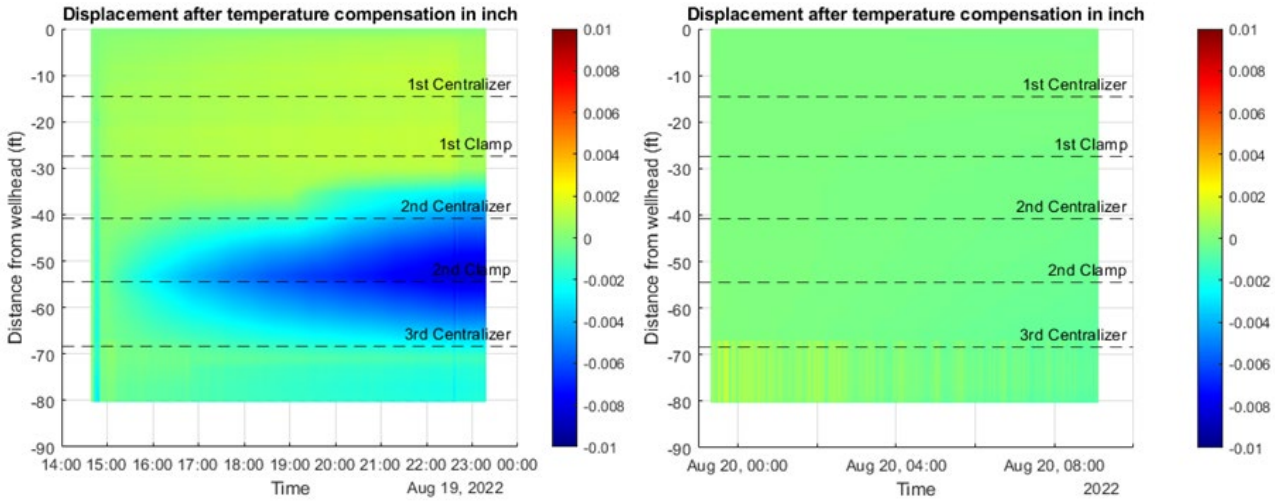

The integrated displacement from the top of the well. Vertical shows the depth and horizontal shows the time in this test. Color bar shows the displacement. Red shows elongation and blue shows shrinkage. (a) shows the displacement during the test and (b) shows the displacement after the test. Both plots show the displacement reference to the beginning of each plot.

Source: LBNL

Field Demonstration

Strain Response During Initial Pressurization

After the tubing was installed and before the valve tree was installed to the wellhead, as required by the California Geologic Energy Management Division, the construction team and PG&E conducted a pressure test to check the integrity of the newly replaced well to make sure the well was sealed properly. DFOS reading was taken in real-time during the pressure test in the annulus and inside the tubing.

The DFOS measurements showed repeatable displacements in both pressure cycles, with or without pressure (Figure 21). When both the annulus and tubing were depressurized, the displacement at all depths was close to 0 millimeters, indicating that the optical fiber cable did not move and returned to its original position. However, when the annulus was pressurized, the tubing was under tension. This could be due to the high pressure in the annulus that pushed the packer to move down; thereby, elongating the tubing and DFOS. Another possible reason for this tension is that when the annulus was under high pressure, the tubing was squeezed in the radial direction, resulting in elongation due to Poisson's effect.

When the tubing was pressurized, the readings indicated a negative displacement, which suggests that the tubing had shortened at all depths. This could be attributed to the increase in pressure inside the tubing, which caused it to expand radially, and due to the Poisson's ratio, the tubing contracted axially. However, since the pressure increase inside the tubing did not displace the packer, the measured displacement was smaller than the displacement observed when the annulus was pressurized.

The difference between the solid and dash lines indicates the difference in relaxation between the tubing and annulus in the second pressure cycle compared to the first pressure cycle.

Figure 21: Displacement of Each Reading During the Field Pressurization Test

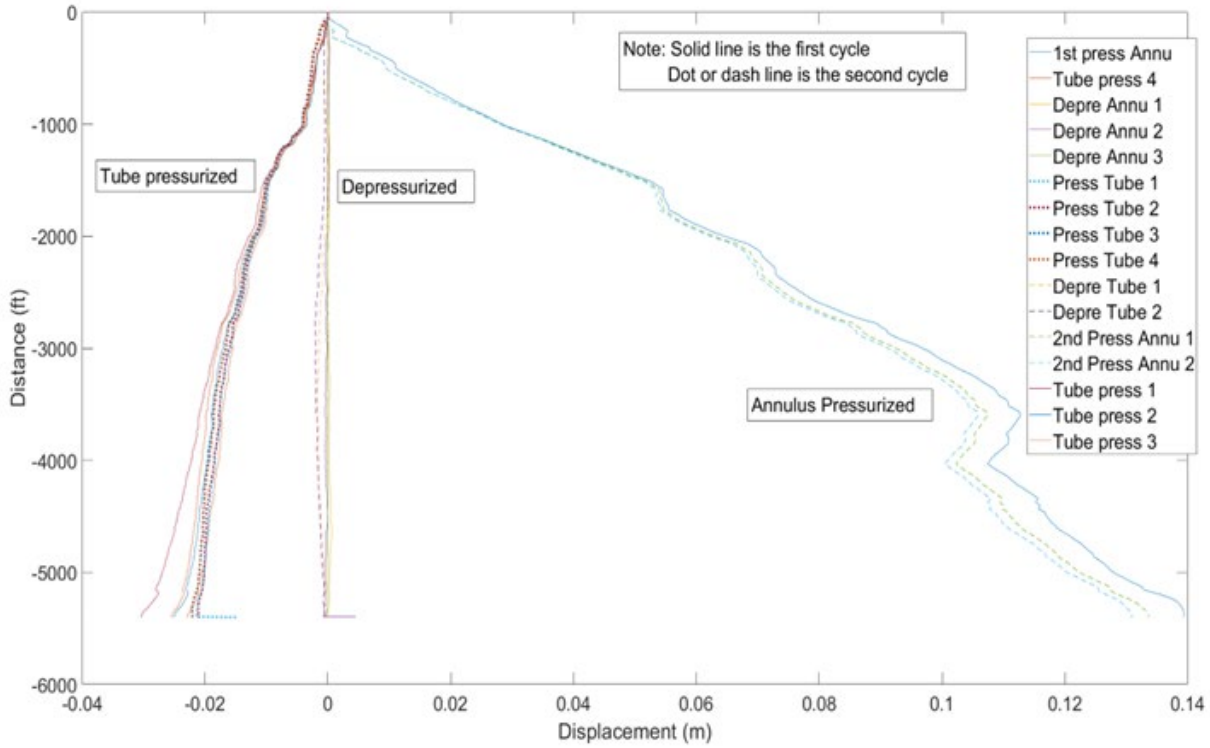

Source: LBNL

Notably, the displacement lost linearity at certain depths, such as around 1,500 feet, 2,200 feet, and 4,400 feet, and the cause of this non-linearity is still unclear. One potential reason for this is that the tubing changed its orientation by approximately 12 degrees between 1,250 feet and 1,750 feet, which may have resulted in contact between the casing and the centralizer on the tubing. This contact could have created friction when the tubing was moved, particularly preventing elongation in those locations. Another possibility is that the tubing twisted during installation, with the elongation being absorbed by the twisting zone and resulting in less elongation in those locations. These possibilities are currently being analyzed in the modeling process to gain a better understanding.

Continuous Reading

Starting in late November 2021, prior to the well's cleaning and operation, automated temperature and strain readings were collected in alternating intervals. Each reading lasted 15 minutes, and the data collection continued until June 8, 2022. Periods of data disconnection occurred intermittently due to power outages, ranging from two hours to one day in duration. The data was collected at 15-minute intervals along the optical fiber cable, with a spatial resolution of 2 meters and a sampling interval of 20 centimeters, resulting in 8,800 data points per reading, and a data size of 157 kilobytes. The collected data was uploaded to Google Drive in real-time, enabling easy access for data interpretation from anywhere.

The data encompassed five stages:

- Stage 1 - Before well is cleaned: The interrogator began readings after the rig was removed and the well was ready to be cleaned.
- Stage 2 - Well cleaning: The well underwent a cleaning process from December 9, 2021, to January 11, 2022.
- Stage 3 - No operation: After cleaning, no operation was performed in the well, resulting in a "quiet" well.
- Stage 4 - Well under operation: From March 18, 2022, the well resumed normal operation, with special events for testing the DFOS systems on May 11, 2022.
- Stage 5 - Operation stopped, and construction started: On June 8, 2022, the well stopped operation due to site construction, but data collection continued until July 13, 2022.

The data in Figure 22 displays the temperature change from November 30, 2021, to July 13, 2022, referenced to the first data collected on November 30, at midnight. The color scale indicates temperature changes in degrees Fahrenheit (°F), where green indicates no temperature change, dark blue shows negative temperature change, and dark red shows positive temperature change. The distance of 0 feet is at the wellhead.

During stage 1, 3, and 5 when no operation was performed, the collected data exhibited a green color along the optical fiber cable, indicating no temperature change. In contrast, during stage 2, the cleaning process caused a heating effect at the top of the well due to the withdrawal of hot fluid from the bottom to the top, resulting in a red color at the top section. However, as pressure inside the well decreased, the temperature at the bottom of the well decreased, resulting in a blue color.

During stage 4, the well resumed normal operation with gas injection and extraction. The extraction process showed a temperature increase at the middle and top of the well, similar to the well cleaning process. On the other hand, injection resulted in temperature increase only at shallow depths, potentially due to the injected gas being hotter than the ground temperature but cooler than the geothermal temperature at deeper levels. This caused a larger temperature reduction at the bottom of the well and a smaller temperature increase at the top of the well.

Figure 22: Temperature Profile from November 30, 2021, to July 13, 2022

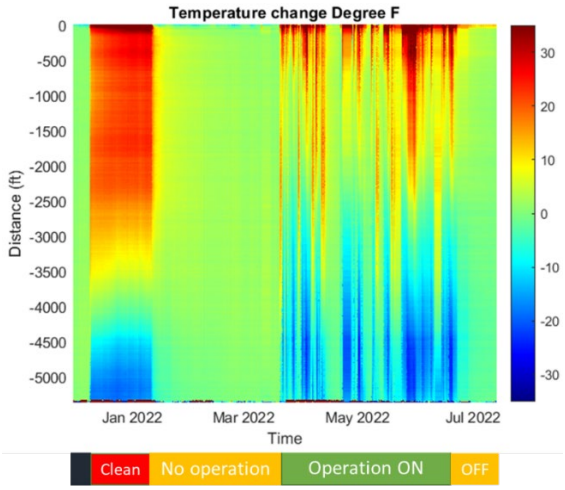

The data are referenced to the first data collected on November 30 at midnight. The color shows the temperature change in degrees Fahrenheit from then on. Green color shows no temperature change. Dark blue shows negative temperature change and dark red shows positive temperature change. Distance 0 ft is at the wellhead.

Source: LBNL

The strain data measured by DFOS was also compared to the pressure and withdrawal rate measured at the flow meter, and the stress changes from March 1 to April 5 are depicted in Figure 23. The power outage period, due to the maintenance of the power supply, is marked in black, and the color range is set to -5 to 5 millipascal (MPa) to improve contrast. The blue solid line at the top represents the withdrawal rate, and the black solid line at the top represents the pressure measured at the gas platform flowmeter. From March 1 to March 18, the fiber showed daily changes of approximately -2 to 2 MPa stress, possibly due to the reaction stress from the daily thermal cycle, resulting in uniform changes throughout the tubing. When the operation commenced with withdrawal (indicated by the left red dashed rectangle), the DFOS showed negative stress in the top 4/5 of the tubing. This occurred again in the middle and right red dashed rectangles, where the negative stress penetrated deep into the borehole. Specifically, for the right rectangle, where the withdrawal rate was high during that time, the strong negative stress reached the bottom of the well.

Figure 23: Stress Distribution Plot with the Pressure, Withdrawal Rate at the Flow Meter from March 1 to April 5

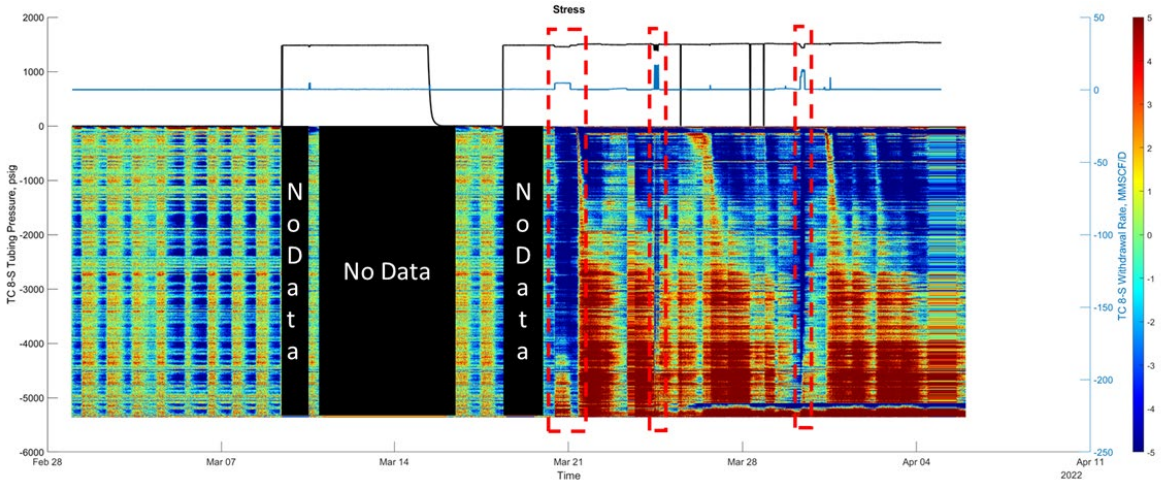

Source: LBNL

In Figure 24, the stress distribution profile is presented at different depths, where blue represents earlier operations, and red indicates later operations. After mid-June, when the operation was halted, the dark red color showed that the stress had returned to near zero by July, except for the area close to the wellhead where the tubing was fixed. Prior to this, the stress ranged between -20 to 20 MPa, except for the region close to the wellhead. At a depth of approximately 5,200 feet, there was another localized stress that showed almost constant negative values after March, suggesting that something had occurred with the DFOS reading. This may be caused by repositioning after several pressure cycles. Since the strain is still small, the deformation is negligible.

Figure 24: Strain Profiles During the Field Demonstration

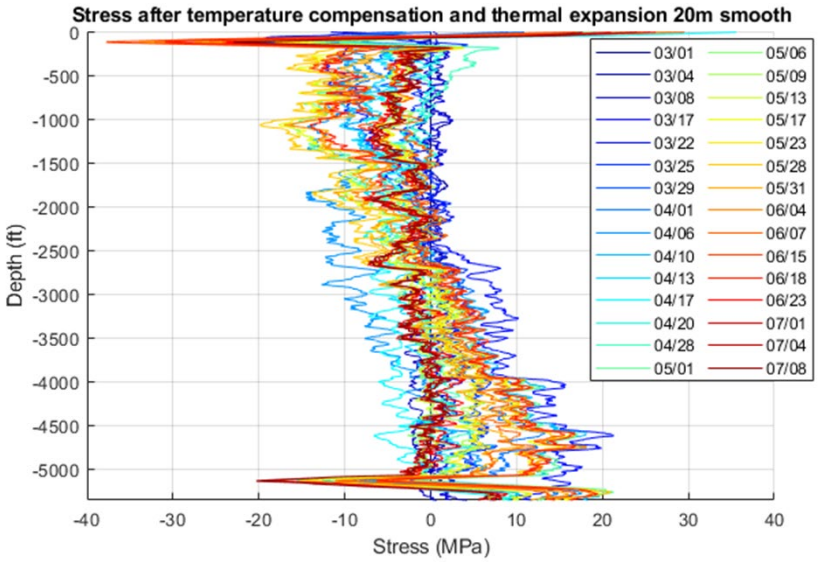

Profiles at different depth every 3 days from March 1 to July 8. The reading on March 1 was the reference. The color from blue to red shows the changes of stress distribution with time.

Source: LBNL

Temperature Logging

Following the completion of construction at the testing site and prior to the resumption of operations, a temperature and noise logging operation was carried out in the testing borehole on November 4, 2022. The temperature and noise logging were performed with both measurements being conducted by a commercial company. At the same time, temperature sensing (DTS) data acquisition was conducted by the research team.

Figure 25 shows the DFOS temperature data, which is in good agreement with the temperature logging data, obtained during the temperature and noise logging performed on November 4, 2022. The temperature in the wellbore exhibited an increasing trend from about 70°F (21°C) at the top to 134°F (57°C) at the bottom. However, some fluctuations were observed in the DFOS temperature data that could be attributed to the temperature variation during the one-hour temperature measurement period. The temperature variation during the test period is also presented, which shows that there was a fluctuation of about one degree Fahrenheit during the temperature and noise logging. Following the unplugging of the logging tools from the well at 12:30 pm, the well temperature experienced a maximum decrease of about two degrees Fahrenheit, which may have resulted from the pressure changes in the well.

Figure 25: Temperature Reading by DFOS and Temperature Logging

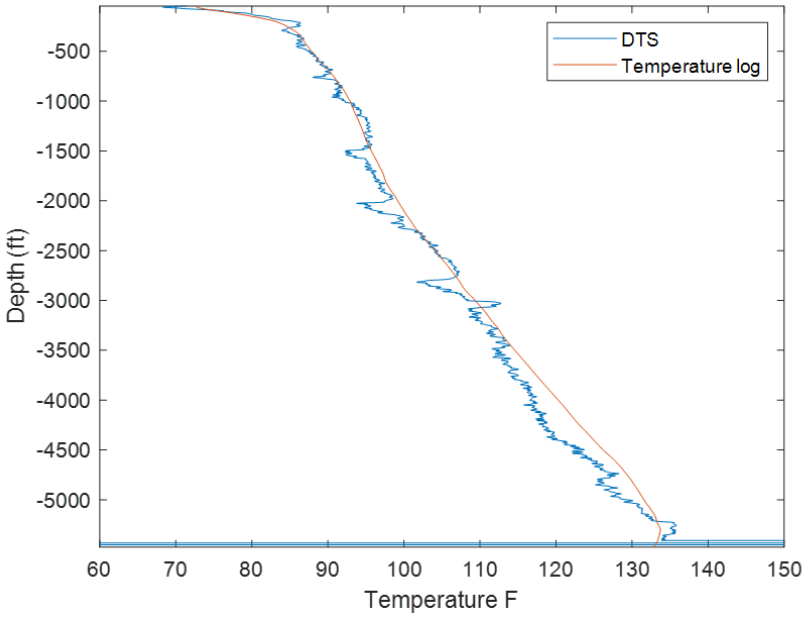

Source: LNBL

EM-TDR

Overview

Due to the inherently one-dimensional nature of EM-TDR measurements, a series of challenges must be addressed to ensure a dependable interpretation.

Primarily, the task involves disentangling electromagnetic reflections from the ambient noise. Employing the stacking method proves effective in mitigating the impact of random noise, thereby enhancing the signal-to-noise ratio. Furthermore, a cross-correlation of the source signal with the raw received signal becomes instrumental in enhancing the true reflections from the surrounding noise. For coherence noise that comes from background radio communications, low-frequency data was used as a calibration tool to distinguish the signals from wellbore reflections and background radio interference noise.

Additionally, meticulous efforts are directed towards minimizing false positives in the interpretation process. Note that this process continued throughout this project and will be further improved in the future. It is established that the resolution of reflected waves is primarily contingent upon the wavelength of the source wavelet, synonymous with the frequency of the emitted waves. Concurrently, the attenuation of waves is determined by the number of cycles during propagation. Consequently, higher-frequency waves exhibit greater attenuation due to a higher number of cycles over the same distance. While higher frequencies are essential in identifying smaller features, they suffer from higher attenuation. In contrast, lower frequencies are adept at distinguishing larger features but exhibit lower attenuation. Given the EM-TDR acquisition covered diverse frequencies, reflections were expected to consistently cover all frequencies or those merging at lower frequencies yet discernible at higher frequencies. Reflections meeting these criteria are deemed likely to originate from actual features, encompassing changes in casing metal (both loss and increase, such as casing joints) and alterations in surrounding dielectric media (for example, water leakage in the surrounding formation, or cement loss). Moreover, various wavelet and spectrum decomposition techniques were employed. The decomposed signal was then filtered, picked, and added back for a cleaner reconstructed signal.

Figure 26 shows an example of the signal decomposition. Here, EM-TDR measured the 5.5-inch casing at the C-FER facility. In this particular example, the data was collected with 1 GHz as the central frequency of the stimulated source signal. The 1-GHz data set has a combination of random electronic noise, background ambient noise, relatively large attenuation due to the high frequency, and potential high resolution. Because the feature distribution is a random event, meaning the reflections from the features would be highly nonlinear. In addition, the 1-GHz frequency range potentially overlaps with the background coherent noise such as microwave or Wi-Fi signal. Due to the high attenuation nature of the 1-GHz signal, the reflections from the near wellhead location may be dominated by the high frequency, whereas the reflections from the locations close to the end of the casing may mainly have lower frequency competent. Consequently, simply applying a frequency-based filter is unlikely to be successful. The main objective is to identify the reflections from the features (specifically, corrosions and metal loss). So, the physical properties that result in the frequency and phase shifting are not the priority currently. Essentially, "oscillations" need to be picked due to the metal loss on the casing instead of the other sources.

Empirical mode decomposition (EMD) was used to separate the useful oscillation information from the noise. This is an approach that is based on wavelet oscillation instead of a frequency-based method. The EMD method decomposes the original into several oscillation modes, which are termed intrinsic mode functions (IMFs). Each of the IMFs represents how fast the

oscillation is. So, smaller features could generate faster oscillation, whereas larger features could generate slower oscillation. In such a method, the trade-off between time and frequency resolution can be overcome that is inherent in the traditional Time-Frequency analysis method due to the Heisenberg uncertainty principle.

In the example shown in Figure 26, the top panel on the left is the raw data. A very strong reflection appeared at the beginning of the data. This is the electromagnetic wave reflected at the top of the casing, specifically, the entry reflection. At around 250 nanoseconds, a low-frequency wide wavelet showed up. Since the casing had fixed length, based on the two-way travel time, the reflections at around 250 nanoseconds are mostly likely from the bottom of the casing. These two reflections are the most distinguishable and easily identified features. The reflected waveform in between these two are either from the reflections from features (metal loss), multiple reflections between features (waves bound multiple times), or artifacts resulting from the noise. In the following panel on the left side of Figure 26, the first five intrinsic mode functions (IMFs) decomposed from the original data. Some of the smaller reflections that are not visible on the original signal are clearly shown on the IMFs. The entry reflections display strong reflections on all the IMFs, this is due to the low attenuation at the beginning of the casing. As a result, all the oscillation modes were preserved in the data. On IMF 5, the reflections from the bottom of the casing are most noticeable compared to other IMFs. This is because the higher number of IMFs tends to preserve the larger oscillation waveform (similar to low-frequency). At the end of the casing, most of the fast oscillation waveforms are attenuated.

Figure 26: EMD Example of 1 GHz Data Collected From the 5.5-inch Well

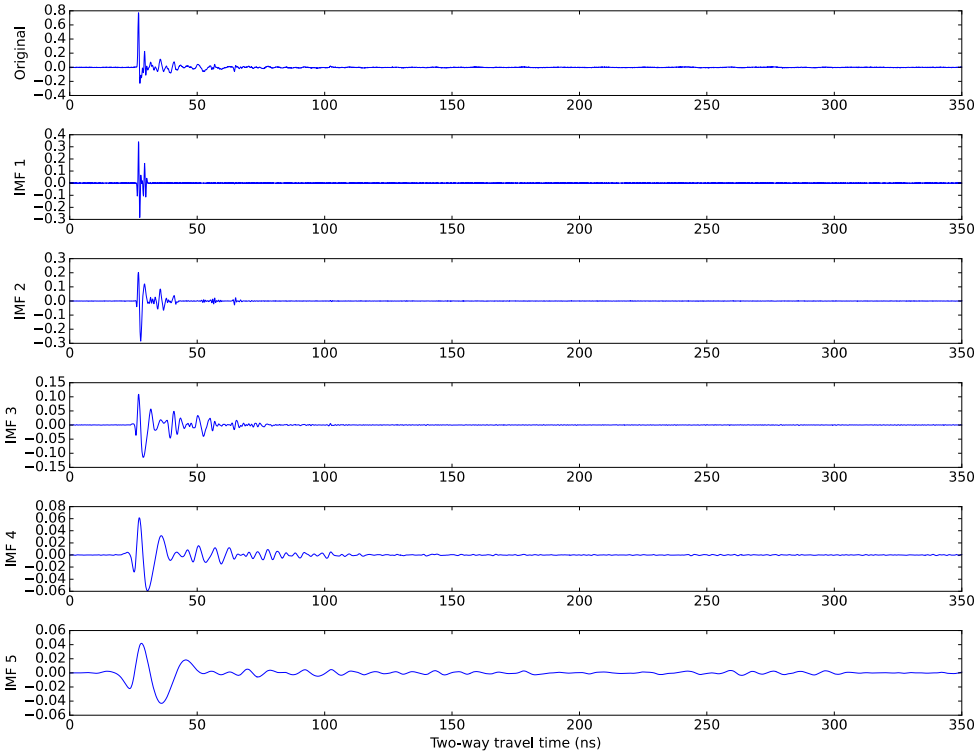

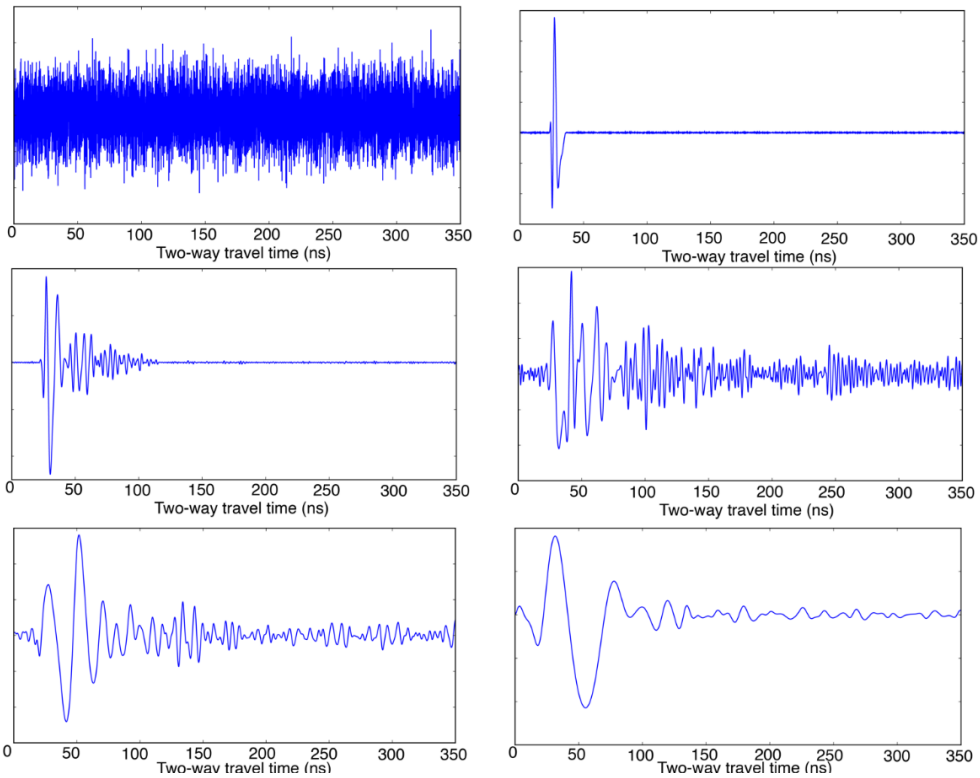

Top: The original signal (top panel) and the sub-sequential IMFs from the EMD (from IMF 1 to IMF 5). Bottom: The additional masked-EMD the IMF 4 into 6 sub-sequential IMFs.

Source: LBNL

Similarly, very finite reflections can be observed in IMF 2, and IMF 3, mostly likely the results of the smaller features (small-size metal loss).

In some of the instances, the EMD is not enough to separate reflections from the different sizes of features and noise, especially if there is coherent noise that has a very similar frequency to the signal. In such cases, applying additional steps of masked EMD or ensemble EMD would be necessary. The details of these techniques are left to references (Gaci, 2016; Wang et al., 2018). The right side of Figure 26 shows an additional masked EMD applied to IMF 4. The original IMF 4 still has fast oscillation noise. After the Masted-EMD, the noise is well separated.

After all these EMD steps, the resulting IMFs were used to identify the potential reflections from the metal losses. The same process was applied to different frequency data sets, using the combined clean IMFs as a reconstructed signal.

EM-TDR Results of the Double-Blind Laboratory Test

The laboratory test is designed to test the EM-TDR method in detecting a variety of features. Figure 27 through Figure 29 demonstrates the statistic pie chart of the features on the 7-inch, 5.5-inch, and 4.5-inch casing strings, respectively.

Figure 27: Feature Distribution Statistics of the 7-inch Casing String

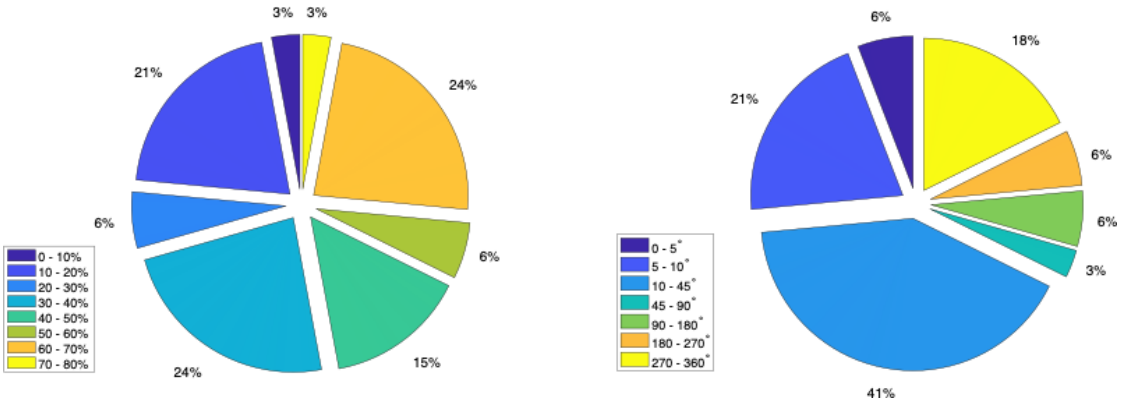

Left: Pie chart depicts the depth distribution of features, represented in terms of thickness percentage. Right: Pie chart illustrates the width distribution of features, represented in terms of circumferential angle.

Source: LBNL

Figure 28: Feature Distribution Statistics of the 5.5-inch Casing String

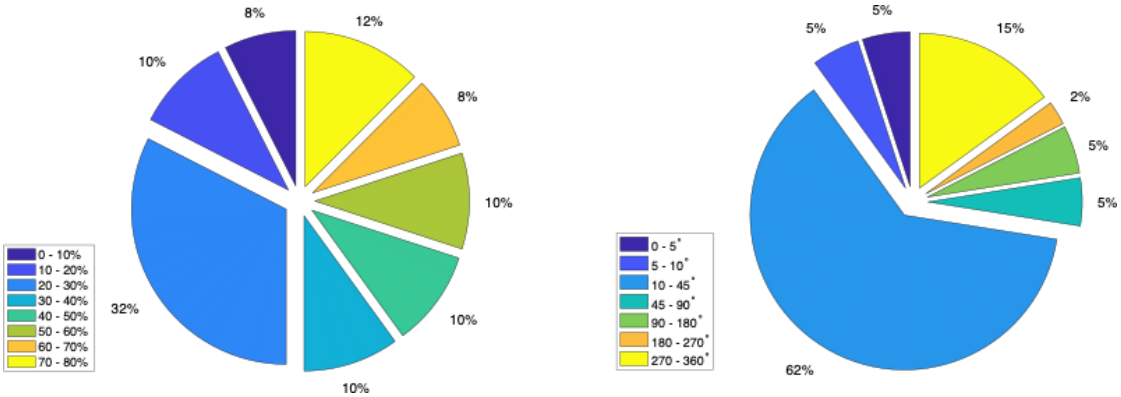

Left: Pie chart depicts the depth distribution of features, represented in terms of thickness percentage. Right: Pie chart illustrates the width distribution of features, represented in terms of circumferential angle.

Source: LBNL

Figure 29: Feature Distribution Statistics of the 4.5-inch Casing String

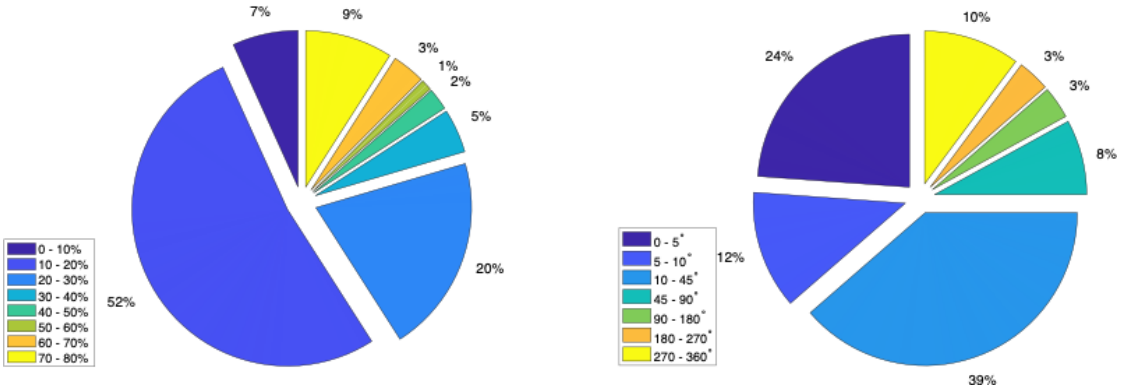

Left: Pie chart depicts the depth distribution of features, represented in terms of thickness percentage. Right: Pie chart illustrates the width distribution of features, represented in terms of circumferential angle.

Source: LBNL

Figures 30 through 32 illustrates the EM-TDR laboratory test results of the 7-inch, 5.5-inch, and 4.5-inch casing at the Deep Well Simulator of C-FER, respectively. Note that these interpretations were the latest ones that improve upon the previous interpretation at the time of the experiment where EMD was not used. The color-coded plots in the top panels are the ground truth after the interpretation. The warmer color represents the deeper metal loss, and vice versa. In the background, the reconstructed EM-TDR signal is represented in envelop form, as an illustration of the reflection power amplitude, in grey scale. The bottom panels display the blue curves are the analytic form of the reconstructed signal overlaying the envelope amplitude form of the reconstructed signal.

As evident in Figures 30a through 32a, the reconstructed EM-TDR signal exhibits a notable correlation with the ground truth across the majority of locations. Notably, this correlation is particularly pronounced in the reflections originating from the vicinity of the wellhead and areas with substantial metal loss. As shown in Figures 30a through 32a, the features in the first segments of all casing strings are predominantly deep and wide-angle metal loss. The EM-TDR signal reflected from these sections not only demonstrates the most significant amplitude, aligning with the observed metal loss but also aligns closely with the boundaries of these features. For instance, in the top panel of Figure 30, at around 10 feet deep of the wellhead, the EM-TDR signal shows a clear correlation with both boundaries of the feature.

While EM-TDR is able to identify the locations of most of the features on the casing strings, due to the limitation of attenuation and wavelength, the exact width of most features is not distinguishable. In the process of mapping the locations of the features, the travel time of the electromagnetic waves in the casing string is assumed to be constant. However, due to the subtle variation in both the casing string and the surrounding media, the speed of the electromagnetic waves may vary. As a result, the identified locations of some of the features are off a bit. For example, from the test result from the 7-inch casing (Figure 30), at around 25 feet from the wellhead, the reflected signal arrived earlier than the actual feature location (the yellow dot in Figure 30a). Furthermore, in sections where features cluster closely, the reflected EM-TDR signals may merge together. Consequently, distinguishing each individual feature becomes challenging in such instances. A noteworthy example is observed in the natural-corrosion section of the 4.5-inch casing string, as depicted in the second section of Figure 32a. Although the EM-TDR signal clearly indicates the presence of a clustered set of features, it is unable to distinctly detect each corrosion feature.

Figure 30: EM-TDR Laboratory Test Results of the 7-inch Casing

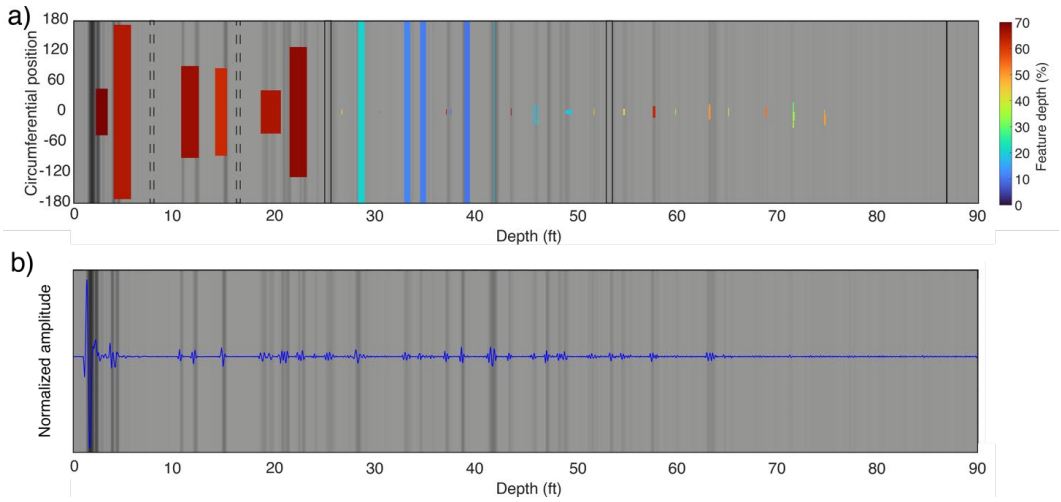

Comparison between the ground truth matrix and the reconstructed EM-TDR signal from the one GHz and two GHz signal on the 7-inch pipe. (a) The ground truth matrix overlays the reconstructed EM-TDR signal in the grey scale. The depth of the feature is represented via the percentage of the pipe thickness in color code. The background reconstructed EM-TDR signal is converted to the envelope form and plotted in the grey scale. The vertical dash lines represent the flush threads that connect pipe module sections. The double solid lines represent the casing joints. The single solid line at the end of the panel represents the end of the pipe. The vertical axis represents the circumferential width of the features (from –180°F [–118°C] to 180°F [82°C]). (b) The reconstructed EM-TDR signal in analytical (blue) form overlays the reconstructed signal in envelope grey scale form (background).

Source: LBNL

Figure 31: EM-TDR Laboratory Test Results of the 5.5-inch Tubing

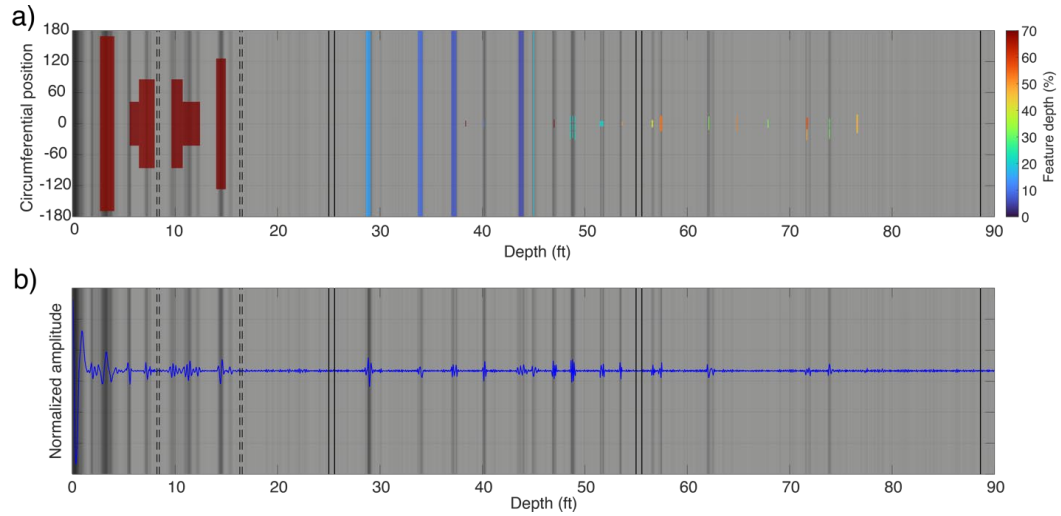

Comparison between the ground truth matrix and the reconstructed EM-TDR signal from the one GHz and two GHz signal on the 5.5-inch pipe. (a) The ground truth matrix overlays the reconstructed EM-TDR signal in the grey scale. The depth of the feature is represented via the percentage of the pipe thickness in color code. The background reconstructed EM-TDR signal is converted to the envelope form and plotted in the grey scale. The vertical dash lines represent the flush threads that connect pipe module sections. The double solid lines represent the casing joints. The single solid line at the end of the panel represents the end of the pipe. The vertical axis represents the circumferential width of the features (from –180°F [–118°C] to 180°F [82°C]). (b) The reconstructed EM-TDR signal in analytical (blue) form overlays the reconstructed signal in envelope grey scale form (background).

Source: LBNL

Figure 32: EM-TDR Laboratory Test Results of the 4.5-inch Tubing

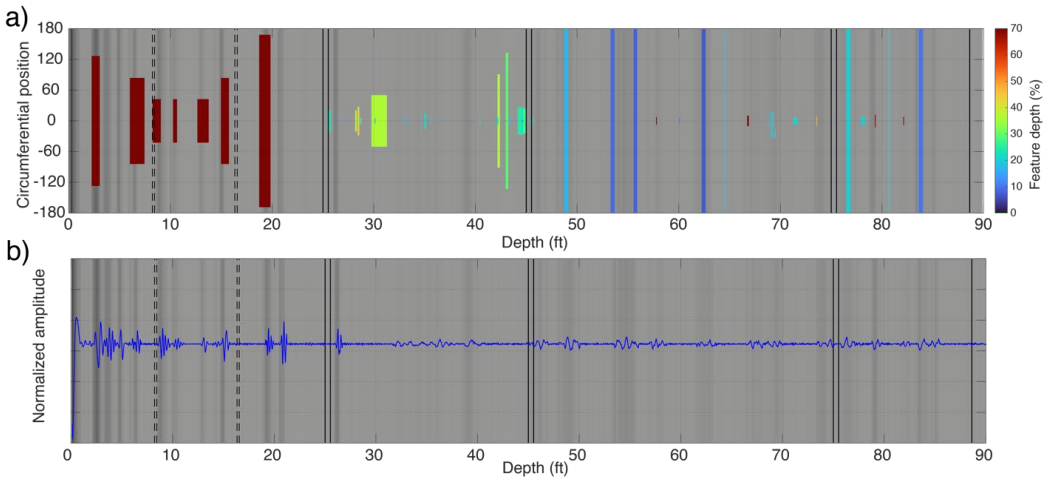

Comparison between the ground truth matrix and the reconstructed EM-TDR signal from the one GHz and two GHz signal on the 4.5-inch pipe. (a) The ground truth matrix overlays the reconstructed EM-TDR signal in the grey scale. The depth of the feature is represented via the percentage of the pipe thickness in color code. The background reconstructed EM-TDR signal is converted to the envelope form and plotted in the grey scale. The vertical dash lines represent the flush threads that connect pipe module sections. The double solid lines represent the casing joints. The single solid line at the end of the panel represents the end of the pipe. The vertical axis represents the circumferential width of the features (from –180°F [–118°C] to 180°F [82°C]). (b) The reconstructed EM-TDR signal in analytical (blue) form overlays the reconstructed signal in envelope grey scale form (background).

Source: LBNL

EM-TDR Results of the Field Test

During the field test, direct access to the ground truth regarding the state of the surface casing is unavailable as it remains within the borehole. Nevertheless, publicly available previous well-logging data was accessed. It is crucial to note that these logging records do not precisely depict the condition of the casing; rather, they provide insights into the characteristics of the geological formation surrounding the casing.

Combining the gamma-ray and the neutron density logging data, several geological layers have different water content. As illustrated in the first green boxes in Figure 33, the first green box seems to have a higher water content, possibly due to the higher porosity of the formation. The second green box shows the formation has relatively lower porosity, possibly due to higher clay or shale content. Both of these layers correlate very well with the EM-TDR data, indicating the EM-TDR signal is also sensitive to the surrounding dielectric media close to the casing. In addition, at the location of the second green box, the EM-TDR data also correlates very well with the geothermal changes, as indicated by the green curve in Figure 33. The green box on the bottom of Figure 33 shows no obvious abnormality from the well logging data, but very good correlation and consistency between different EM-TDR data. It is possible that there are changes in this formation after the well-logging data was acquired and identified by the EM-TDR measurement. Another possibility is that the formation has not changed, but there is some corrosion developing in the casing itself. In order to confirm what is the cause of the EM-TDR reflection at this location, further investigation, such as more recent well logging, or pulling out the casing, is necessary.

There are also some EM-TDR reflections that are shown on some of the frequencies but absent from the others. For the reflections that are not shown in the well-logging data, these are most likely due to the small corrosion in the casing or cracks in the surrounding cement. The indicated results are shown in red boxes in Figure 33. On the other hand, the EM-TDR data shown on the well-logging data are absent from some of the EM-TDR data; they are most likely from the small-scale geological change in the vicinity of the casing. Again, further access to the ground truth is necessary to evaluate the accuracy of EM-TDR interpretation.

Figure 33: Gamma-ray and the Neutron Density Logging Data for the Tested Field Wellbore

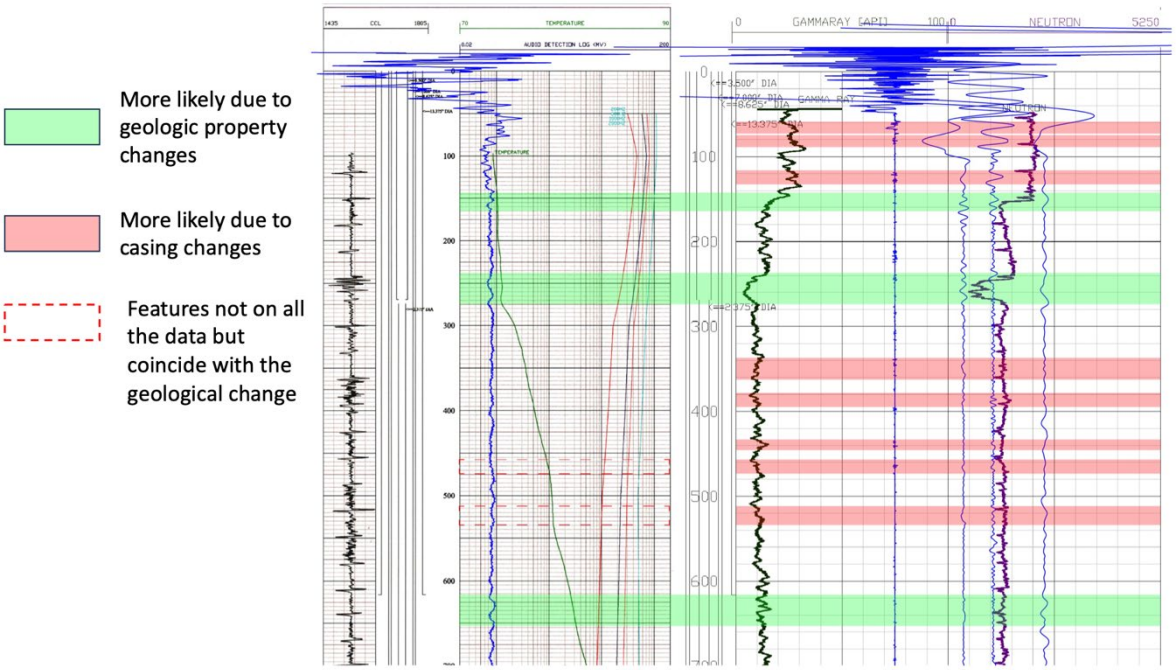

EM-TDR data overlays the previous well-logging data. The blue curves are the EM-TDR data from different frequencies. The surface casing diagram is shown in the middle. The most left logging data is the collar locator data acquired in November 2005. The green curve is the temperature logging data from November 2005. The black curve in the middle is the Gamma-ray log data acquired in March 2013. The purple curve is the neutron density log data acquired in March 2013. The color-coded horizontal boxes are the interpretation of the cause of the correlation between EM-TDR data and the previous well-logging data.

Source: PG&E

CHAPTER 4: Conclusion

This report serves to illustrate the precision and viability of DFOS and EM-TDR technology in distribution UGS well integrity monitoring.

DFOS is a promising method of monitoring the UGS wells to detect corrosion occurring on the inner tubing or outer casing. Traditional sensors can only assist in determining whether there is potential corrosion around their installation locations. It also demonstrates its capability to identify and localize deformation on the tubing, casing, and even the cement behind the casing, depending on where the optical fiber cable is installed. The results show that the optical fiber cable can locate leakage-related temperature events and detect minor deformations under pressure cycles if a tight buffer cable is properly installed to transfer the strain in the well to the cable.

The field demonstration included the installation and monitoring of a homemade distributed fiber optic temperature and strain sensing system. The analyzer performed reliably throughout the entire demonstration period. The low-cost analyzer was designed to operate in real-time and stream the recorded data to the cloud, which could be accessed remotely. The system was able to provide strain and temperature data that could be pre-processed, eliminating the need for additional computational processing, and allowing for real-time interpretation by engineers. Additionally, this system required less data storage compared to other distributed fiber optic sensing technologies.

Using the combined DSS and DTS interrogator, the system was able to monitor the operation of the well in real-time, providing temperature and strain profiles at all depths along the storage well of 5,500 feet deep with a spatial interval of 20 centimeters, a 10-minute data update rate, and a resolution of less than 34°F (1°C) or 20 microstrain. The temperature and strain data collected by the system indicated the injection and extraction operations in the storage well and showed a correlation with the flow rate and pressure at the flow meter. By converting the strain data to displacement, the deformation of the well could also be observed. Over a longer monitoring period, after multiple pressure cycles, the stress/displacement profile could potentially help build a dataset of the normal stress and deformation of the tubing.

This technology has significant potential for integrity monitoring in the long-term, as the current datasets, especially the stress response data, can serve as a reference when the tubing becomes old, and deformation becomes a concern in the future. By plotting the pressure and stress over time, the location of potential damage can be predicted before encountering a real problem with the tubing. Overall, this system offers a low-cost solution for real-time monitoring of tubing integrity, which could help prevent catastrophic failures leading to environmental damage and costly repairs.

However, to achieve accurate monitoring results, certain requirements for the cable layout must be met. To better capture temperature changes caused by pressure variations, the temperature-sensitive fiber should be positioned close to the tubing wall and firmly attached.

Considering that the potential corrosion area might be very small, increasing the number of cables in the circumferential direction would be more conducive to detecting the corrosion area.

DFOS has limitations, particularly at risk of missing small areas of corrosion if the optical fiber is not aligned with the damaged area. However, EM-TDR has shown promise in overcoming these limitations. Through double-blind laboratory tests, we have demonstrated this technology's potential for its accuracy in locating and evaluating casing damages, including challenging scenarios characterized by densely distributed features, as demonstrated by the C-FER tests. In the field test, where direct access to ground truth is unavailable, correlations between the EM-TDR signal and previous well-logging data were observed. This underscores the technology's potential not only in wellbore integrity investigations but also in effectively monitoring the surroundings of the casing. EM-TDR also offers the unprecedented advantage of not needing any downhole installation or even the opening of the wells, making it a true non-invasive and non-interruptive method for borehole integrity monitoring for deep storage wells. Such an innovative tool does not exist on the market.

While EM-TDR technology does not offer a comprehensive three-dimensional depiction of wellbore conditions, its utility lies in its rapid and non-intrusive investigative capabilities. During the field test at the PG&E gas facility, measurements were conducted without the need to open the wellhead. Moreover, due to the fact that electromagnetic waves propagate at speeds approaching that of light, a single measurement, even with a 300-time stacking process, only requires a matter of minutes, ensuring a highly time-efficient process. Furthermore, the EM-TDR method, rooted in the transmission of electromagnetic waves through metallic media, renders it readily applicable to pipeline integrity monitoring.

Preserving the integrity of energy infrastructure and reducing monitoring costs is paramount for the advancement of sustainable energy in alignment with California's clean energy and climate objectives. By applying EM-TDR technology to both wellbore and pipeline contexts, it emerges as a swift screening tool for energy infrastructure maintenance, integrity assessments, and leakage mitigation. Functioning as a supplementary tool alongside existing high-resolution imaging/logging methods, EM-TDR is particularly suited for routine, expedited monitoring. As the degradation progresses and reaches a predefined threshold, as signaled by the EM-TDR survey, the implementation of more detailed and intrusive high-resolution logging/imaging tools becomes necessary.

As highlighted in this report, the EM-TDR method is currently in its initial stages of development. Numerous challenges, both recognized and unforeseen, persist in real-world scenarios, encompassing issues like ambient noise interference and complex reflections arising from intricate, complex pipeline or casing geometries (such as pipeline loops and borehole connections). Moreover, physical properties in the surrounding geological formation can impact EM-TDR signals. To enhance the comprehension of EM-TDR's utility and sensitivity, further laboratory tests, particularly those exploring distance and damage size sensitivity, are imperative. Conducting additional field tests, supported by ground truth data, would significantly contribute to calibration efforts.

GLOSSARY AND LIST OF ACRONYMS

Term	Definition
BOTDR	Brillouin optical time domain reflectometry
°C	degrees Celsius
C-FER	C-FER Technologies
DAS	distributed acoustic sensing
DFOS	distributed fiber optic sensing
DSS	distributed strain sensing
DSTS	distributed strain and temperature sensing
DTS	distributed temperature sensing
EMD	empirical mode decomposition
EM-TDR	electromagnetic time domain reflectometry
°F	degrees Fahrenheit
FC/ACP	fixed connection angled physical contact
FIMT	Fiber In Metal Tube
GHz	gigahertz
IMF	intrinsic mode function
kN	kilonewton
LBNL	Lawrence Berkeley National Laboratory
MHz	megahertz
MHz/%	megahertz per percent
MHz/°C	megahertz per degree Celsius
MPa	millipascal
PG&E	Pacific Gas and Electric Company
psi	pounds per square inch
UGS	underground gas storage

References

Al-Hussain, Ali Musa, M. Enamul Hossain, Abdulazeez Abdulraheem, and Rahul Gajbhiye. 2015. "An Integrated Approach for Downhole Leak Detection," in *SPE Saudi Arabia Section Annual Technical Symposium and Exhibition*, Al-Khobar, Saudi Arabia. April 21, 2015. 21–23. Available at: https://doi.org/10.2118/177996-MS.

Al-Zain, Ahmed, Abdullah Al-Mulhim, Fehead Al-Subaie, Ahmed Al-Jandal, Abdul-Aziz Al-Mulhem, and Omar Al-Hindas. 2016. "Well Integrity Assessment Using Video Camera Technology-Case Histories," in *Abu Dhabi International Petroleum Exhibition & Conference,* Abu Dhabi, United Arab Emirates. November 7, 2016. 1–8. Available at: https://doi.org/10.2118/182952-MS.

Amir, N., O. Barzelay, A. Yefet, and T. Pechter. October 1, 2009. "Condenser Tube Examination Using Acoustic Pulse Reflectometry." ASME. J. Eng. Gas Turbines Power. January 2010; 132(1): 014501. https://asmedigitalcollection.asme.org/gasturbinespower/article-abstract/132/1/014501/409227/Condenser-Tube-Examination-Using-Acoustic-Pulse?redirectedFrom=PDF

Assous, Said, James Whetton, and Mark Bacciarelli. 2021. "Magnetic Flux Leakage Data Processing for Casing Inspection: An Inversion Approach," in *International Petroleum Technology Conference*, Virtual, March 16, 2021. 1–10. Available at: https://doi.org/10.2523/IPTC-21167-MS.

Braga, A.M., H.L. Pinto, and P. Gouvea. 2013. "Well Integrity Monitoring: Challenges and Perspectives," in *Offshore Technology Conference Brasil,* Rio de Janeiro, Brazil. October 29, 2013. Available at: https://doi.org/10.4043/24515-MS.

Conley, S., G. Franco, I. Faloona, D.R. Blake, J. Peischl, and T.B. Ryerson. 2016. "Methane emissions from the 2015 Aliso Canyon blowout in Los Angeles, CA." *Science*, 351(6279), 1317–1320. Available at: https://doi.org/10.1126/science.aaf2348.

Cornot-Gandolphe, Sylvie. 2013. *Underground Gas Storage in the World 2013 (fifth edition)*. Centre International d'Information sur le Gaz Naturel et tous Hydrocarbures Gazeux. Report Number: INIS-FR-15-0533. France. June 15, 2013. Available at: https://www.osti.gov/etdeweb/biblio/22376367.

Freifeld, B., C. Oldenburg, P. Jordan, L. Pan, S. Perfect, J. Morris, J. White, S. Bauer, D. Blankenship, B. Roberts, G. Bromhal, D. Glosser, D. Wyatt, and K. Rose. 2016. *Well Integrity for Natural Gas Storage in Depleted Reservoirs and Aquifers*. United States Department of Energy, National Energy Technology Laboratory. Report Number NETL-TRS-15-2016. December 16, 2016. 1–84. Available at: https://netl.doe.gov/projects/files/WellIntegrityforNaturalGasStorageinDepletedReservoirsandAquifers_121616.pdf.

Furse, Cynthia, Paul Smith, and Michael Diamond. 2009. "Feasibility of Reflectometry for Nondestructive Evaluation of Prestressed Concrete Anchors." *IEEE Sensors Journal*, 9(11), 1322–1329. Available at: https://doi.org/10.1109/JSEN.2009.2019309.

Gaci, Said. 2016. "New Ensemble Empirical Mode Decomposition (EEMD) Denoising Method for Seismic Signals." *Energy Procedia*, 97, 84–91. Available at: https://doi.org/10.1016/j.egypro.2016.10.026.

Guo, Zhen, Gaoce Han, Jize Yan, David Greenwood, James Marco, and Yifei Yu. 2021. "Ultimate Spatial Resolution Realisation in Optical Frequency Domain Reflectometry with Equal Frequency Resampling." *Sensors*, 21(14), 4632. Available at: https://doi.org/10.3390/s21144632.

Heimovaara, T.J. 1993. "Design of Triple-Wire Time Domain Reflectometry Probes in Practice and Theory." *Soil Science Society of America Journal*, 57(6), 1410–1417. Available at: https://doi.org/10.2136/sssaj1993.03615995005700060003x.

Herkelrath, W.N., S.P. Hamburg, and F. Murphy. 1991. "Automatic, Real-Time Monitoring of Soil Moisture in a Remote Field Area with Time Domain Reflectometry." *Water Resources Research*, 27(5), 857–864. Available at: https://doi.org/10.1029/91WR00311.

Kiran, Raj, Catalin Teodoriu, Younas Dadmohammadi, Runar Nygaard, David Wood, Mehdi Mokhtari, and Saeed Salehi. 2017. "Identification and evaluation of well integrity and causes of failure of well integrity barriers (A review)." *Journal of Natural Gas Science and Engineering*, 45, 511–526. Available at: https://doi.org/10.1016/j.jngse.2017.05.009.

Lubinski, A., and W.S. Althouse. 1962. "Helical Buckling of Tubing Sealed in Packers." *Journal of Petroleum Technology*, 14(06), 655–670. Available at: https://doi.org/10.2118/178-PA.

Luna Innovation Inc. 2020. *Optical Distributed Sensor Interrogator Model ODiSI 6: User's Guide*. 1–98. Available at: https://lunainc.com/sites/default/files/assets/files/resource-library/ODiSI%206100%20User%20Guide.pdf.

Luo, Luo, Paolo Ferracin, Jillian Stern, Danko van der Laan, Xiaorong Wang, Jeremy Weiss, and Yuxin Wu. 2022. "Distributed Fiber Optic Sensing to Identify Locations of Resistive Transitions in REBCO Conductors and Magnets." *IEEE Transactions on Applied Superconductivity*, 32(6), 1–6. Available at: https://doi.org/10.1109/TASC.2022.3159507.

Miyazaki, Brent. 2009. "Well integrity: An overlooked source of risk and liability for underground natural gas storage. Lessons learned from incidents in the USA." *Geological Society, London, Special Publications*, 313(1), 163–172. Available at: https://doi.org/10.1144/sp313.11.

Mohammed, Auwalu I., Babs Oyeneyin, Bryan Atchison, and James Njuguna. 2019. "Casing structural integrity and failure modes in a range of well types - A review." *Journal of*

Natural Gas Science and Engineering, 68, 102898. Available at: https://doi.org/10.1016/j.jngse.2019.05.011.

Nagel, N.B. 2001. "Compaction and subsidence issues within the petroleum industry: From Wilmington to Ekofisk and beyond." *Physics and Chemistry of the Earth, Part A: Solid Earth and Geodesy*, 26(1–2), 3–14. Available at: https://doi.org/10.1016/S1464-1895(01)00015-1.

Ojeda, V.A., L. Lázaro, J.J. Benito, and J.M. Bastidas. 2016. "Assessment of cathodic protection by close interval survey incorporating the instant off potential method." *Corrosion Engineering, Science and Technology*, 51(4), 241–247. Available at: https://doi.org/10.1179/1743278215Y.0000000041.

Peng, Xiang, Uchenna Anyaoha, Zheng Liu, and Kazuhiko Tsukada. 2020. "Analysis of Magnetic-Flux Leakage (MFL) Data for Pipeline Corrosion Assessment." *IEEE Transactions on Magnetics*, 56(6), 1–15. Available at: https://doi.org/10.1109/TMAG.2020.2981450.

Roman, Muhammad, Damilola Balogun, Yiyang Zhuang, Rex E. Gerald II, Laura Bartlett, Ronald J. O'Malley, and Jie Huang. 2020. "A Spatially Distributed Fiber-Optic Temperature Sensor for Applications in the Steel Industry." *Sensors*, 20(14), 1–20. Available at: https://doi.org/10.3390/s20143900.

Rouhbakhsh Arfaee, Mohammad Iman, and Behnam Sedaee Sola. 2014. "Investigating the effect of fracture–matrix interaction in underground gas storage process at condensate naturally fractured reservoirs." *Journal of Natural Gas Science and Engineering*, 19, 161–174. Available at: https://doi.org/10.1016/j.jngse.2014.05.007.

Sasaki, T., J. Park, K. Soga, T. Momoki, K. Kawaguchi, H. Muramatsu, Y. Imasato, A. Balagopal, J. Fontenot, and T. Hall. 2019. "Distributed fibre optic strain sensing of an axially deformed well model in the laboratory." *Journal of Natural Gas Science and Engineering*, 72, 103028. Available at: https://doi.org/10.1016/j.jngse.2019.103028.

Sasaki, T., S. Zhang, K. Soga, L. Luo, B. Freifeld, Y. Kitayama, K. Kawaguchi, and H. Sugiyama. 2021. "Distributed fiber optic strain sensing of bending deformation of a well mockup in the laboratory." *Journal of Natural Gas Science and Engineering*, 96, 104309. Available at: https://doi.org/10.1016/j.jngse.2021.104309.

Schwall, G.H. and C.A. Denney. 1994. "Subsidence Induced Casing Deformation Mechanisms in the Ekofisk Field," in *Rock Mechanics in Petroleum Engineering*, Delft, Netherlands. August 29, 1994. Available at: https://doi.org/10.2118/28091-MS.

Silva, M.F., K.M. Muradov, and D.R. Davies. 2012. "Review, Analysis and Comparison of Intelligent Well Monitoring Systems," in *SPE Intelligent Energy International*, Utrecht, Netherlands. March 27, 2012. Available at: https://doi.org/10.2118/150195-MS.

Topp, G.C., and J.L. Davis. 1985. "Measurement of Soil Water Content using Time-domain Reflectometry (TDR): A Field Evaluation." *Soil Science Society of America Journal*, 49(1), 19–24. Available at: https://doi.org/10.2136/sssaj1985.03615995004900010003x.

U.S. DOE (United States Department of Energy). 2016. *Ensuring Safe and Reliable Underground Natural Gas Storage: Final Report of the Interagency Task Force on Natural Gas Storage Safety*. United States Department of Energy. October 2016. Available at: https://www.energy.gov/sites/prod/files/2016/10/f33/Ensuring%20Safe%20and%20Reliable%20Underground%20Natural%20Gas%20Storage%20-%20Final%20Report.pdf.

Wang, Jiannan, Robert R. Stewart, Nikolay I. Dyaur, and M. Lee Bell. 2016. "Marine guided waves: Subbottom property estimation and filtering using physical modeling data." *Geophysics*, 81(4), IJA–Z38. Available at: https://doi.org/10.1190/geo2015-0401.1.

Wang, Jiannan, and Yuxin Wu. 2020. "Wellhead based time domain reflectometry for casing integrity investigation." *International Journal of Greenhouse Gas Control*, 96, 103002. Available at: https://doi.org/10.1016/j.ijggc.2020.103002.

Wang, Xiuli, and Michael Economides. 2009. "Chapter 8 - Underground Natural Gas Storage." *Advanced Natural Gas Engineering*. Gulf Publishing Company. 289–302. ISBN 978-1933762388. Available at: https://doi.org/10.1016/b978-1-933762-38-8.50015-0.

Wang, Yung-Hung, Kun Hu, and Men-Tzung Lo. 2018. "Uniform Phase Empirical Mode Decomposition: An Optimal Hybridization of Masking Signal and Ensemble Approaches." IEEE Access 6 (January): 34819–33. https://www.ncbi.nlm.nih.gov/pmc/articles/PMC6521981/

Zhang, Y., C.M. Oldenburg, Q. Zhou, L. Pan, B.M. Freifeld, P. Jeanne, V.R. Tribaldos, and D.W. Vasco. 2022. "Advanced monitoring and simulation for underground gas storage risk management." *Journal of Petroleum Science and Engineering*, 208(E), 109763. Available at: https://doi.org/10.1016/j.petrol.2021.109763.

Project Deliverables

The Project Deliverables, including interim and final reports are listed below in alphabetic order:

- C-FER test report
- Controlled experiment plan
- Demonstration plan
- Fiber optic cable test results
- Fiber test plan
- Field demonstration report
- Field installation plan
- Lab evaluation report
- Lab test plan
- Numerical model report
- Technical evaluation report